Identification of the Highly Active Co-N_4 Coordination Motif for Selective Oxygen Reduction to Hydrogen Peroxide

Shanyong Chen[1,2,‡], Tao Luo[1,‡], Xiaoqing Li[1], Kejun Chen[1], Junwei Fu[1], Kang Liu[1], Chao Cai[1], Qiyou Wang[1], Hongmei Li[1], Yu Chen[1], Chao Ma[3], Li Zhu[4], Ying-Rui Lu[5], Ting-Shan Chan[5], Mingshan Zhu[2,*], Emiliano Cortés[4,*], Min Liu[1,*]

[1] Hunan Joint International Research Center for Carbon Dioxide Resource Utilization, State Key Laboratory of Powder Metallurgy, School of Physical and Electronics, Central South University, 410083 Changsha, China.

[2] Guangdong Key Laboratory of Environmental Pollution and Health, School of Environment, Jinan University, 511443 Guangzhou, China.

[3] School of Materials Science and Engineering, Hunan University, Changsha, 410082, China

[4] Nanoinstitut München, Fakultät für Physik, Ludwig-Maximilians-Universität München, 80539 München, Germany.

[5] National Synchrotron Radiation Research Center, Hsinchu, 30076, Taiwan.

‡ These authors contributed equally.

*e-mails: zhumingshan@jnu.edu.cn, emiliano.cortes@lmu.de, minliu@csu.edu.cn

Table of Contents

Experimental Section

Chemicals. Cobaltous nitrate hexahydrate ($Co(NO_3)_2 \cdot 6H_2O$), cobalt phthalocyanine ($C_{32}H_{16}CoN_8$), 4-dimethylaminopyridine ($C_7H_{10}N_2$), dicyandiamide ($C_2H_4N_4$), 2-methylimidazole ($C_4H_6N_2$), methyl blue ($C_{37}H_{27}N_3Na_2O_9S_3$), N,N-Dimethylformamide (DMF), and potassium thiocyanate (KSCN) were purchased from Shanghai Aladdin Bio-Chem Technology. Carbon ECP600JD was obtained from Lion Corporation Japan. Nafion solution (5 wt. %) was purchased from Alfa Aesar China. All chemicals were directly used without further purification.

Synthesis of Co-N SAC_{Dp}. Typically, 0.75 g of $C_7H_{10}N$ (4-dimethylaminopyridine) was dissolved into deionized water (10 mL) after ultrasonic treatment for 10 min. Then 0.06 g of $Co(NO_3)_2 \cdot 6H_2O$ (cobaltous nitrate hexahydrate) and 0.15 g of ECP600JD (carbon black) were successively added into the clear $C_7H_{10}N$ solution under ultrasonication. After stirring for 10 h at room temperature, the above-mixed solution underwent rotary evaporation treatment to obtain the black mixture powder. Then, the black mixture powder was calcined at 800 ºC for 2 h under N_2 protection with the rising temperature rate of 3 ºC/min. The obtained powders were soaked in 1 M HCl solution at 80 °C under continuous stirring for 12 h to remove the Co nanoparticle. Lastly, after washing with water and ethanol through filtration, the precipitate was collected and dried at 60 °C for 18 h, and the Co-N SAC_{Dp} was obtained. For Co-N SAC_{Dp}-700 and Co-N SAC_{Dp}-900 samples, the synthesis process is the same as that of Co-N SAC_{Dp}, but the calcination temperature is 700 ºC and 900 ºC, respectively. The CN was prepared as a similar procedure with the Co-N SAC_{Dp} without the addition of Co salts and the acid etching process. The Co-N SAC_{Dp} is subjected to the H_2 reduction treatment (450 ºC, 2h, 5% H_2 in Ar), which is denoted as Co-N SAC_{Dp}-H_2.

Synthesis of Co-N SAC_{Mm}. Typically, 0.75 g of $C_4H_6N_2$ (2-methylimidazole) was dissolved into deionized water (10 mL) after ultrasonic treatment for 10 min. Then 0.02 g of $Co(NO_3)_2 \cdot 6H_2O$ (cobaltous nitrate hexahydrate) and 0.15 g of ECP600JD (carbon black) were successively added into the clear $C_4H_6N_2$ solution under ultrasonication. After stirring for 10 h at room temperature, the above-mixed solution underwent rotary evaporation treatment to obtain the black mixture powder. Then, the black mixture powder was calcined at 750 ºC for 2 h under N_2 protection with the rising temperature rate of 3 ºC/min. After acid etching treatment with 1M HCl, the Co-N SAC_{Mm} was obtained.

Synthesis of Co-N SAC_{Pc}. Typically, 0.7 g of $C_2H_4N_4$ (dicyandiamide) was dissolved into DMF (10 mL) after ultrasonic treatment for 10 min. Then 0.04 g of $C_{32}H_{16}CoN_8$ (cobalt phthalocyanine) and 0.16 g of ECP600JD (carbon black) were successively added into the clear $C_2H_4N_4$ solution under ultrasonication. After stirring for 6 h at room temperature, the above-mixed solution underwent rotary evaporation treatment to obtain the black mixture powder. Then, the black mixture powder was calcined at 800 ºC for 2 h under N_2 protection with the rising temperature rate of 3 ºC/min. After acid etching treatment with 1M HCl, the Co-N SAC_{Pc} was obtained.

Characterization. Raman spectra were recorded on a Laser Micro-Raman Spectrometer (Renishaw InVia, UK). Powder X-ray diffraction (XRD) patterns were collected from the D8 advance X-ray diffractometer (Cu Kα radiation, λ = 1.54 Å,

Rigaku). Scanning electron microscopy (SEM) images were acquired from the TESCAN MIRA3 field emission scanning electron microscopy (LMH). Transmission electron microscopy (TEM), high-angle annular dark-field-TEM (HAADF-TEM), and element mapping images were obtained from a Titan G2 60–300 microscope. The AC-HAADF-STEM images were collected from a JEOL ARM200F microscope with a probe-forming spherical aberration corrector. The Fourier transform infrared (FT-IR) spectra were acquired from a Thermo Fisher Nicolet Is5 with transmission mode. The nitrogen adsorption-desorption isotherm measurements were carried out on the Micromeritics ASAP 2020. The specific surface area and pore distribution were analyzed based on Brunauer–Emmett–Teller (BET) method and Barrett-Joyner-Halenda (BJH) model, respectively. UV-Vis spectra were obtained from the Shimadzu UV-2600. X-ray photoelectron spectroscopy (XPS) measurements were performed on a Thermo Scientific K-Alpha (Al Kα radiation, hν=1486.6 eV) and all the binding energies are corrected by the C 1s peak of 284.8 eV. The XAS spectra were measured on a hard X-ray spectrometer at the TLS 01C1 and TLS 16A1 beamlines of the National Synchrotron Radiation Research Center (NSRRC, Taiwan) in the fluorescence mode. The corresponding XAFS data were analyzed through the standard procedures using the Ifeffit package[1]. The O_2 TPD spectra are collected on the chemisorption analytical instrument of PCA-1200 (BEIJING BUILDER ELECTRONIC TECHNOLOGY CO.,LTD).

Electrochemical ORR measurement. The electrochemical ORR was measured on a CHI760E Electrochemical Workstation (CH Instruments) with a three-electrode configuration electrochemical cell. The graphite rod and Ag/AgCl electrode were chosen as the counter electrode and reference electrode, respectively. The rotating ring disk electrode with an electrode area of 0.2475 cm^2 (RRDE, PINE Research Instrumentation) was used as the working electrode. In the preparation process of a catalyst ink, 4 mg of the catalyst and 30 μL of Nafion solution (5 wt. %) were mixed with water/ethanol solution (V_{water}= 100 μL; $V_{ethanol}$=870 μL) and then were dispersed by ultrasonication for 1 h to obtain a homogeneous ink. Next, 5 μL of the ink was dropped on the polished RRDE and dried at room temperature.

Before the ORR, the pre-activation process by scanning cycle voltammetry (CV) curves (40 cycles, scan rate: 50 mV/s) was performed on RRDE to electrochemically clean it until stable CV curves were obtained. The ORR polarization curves were acquired from linear sweep voltammograms (LSV) measurement with the sweep speed of 10 mV s^{-1} at 1600 rpm in O_2 purified electrolyte, and Pt ring potential was maintained at 1.2 V (vs. RHE) to respond to the generated H_2O_2. Especially, the electrochemical clean process for Pt ring was carried out through scanning CV curves for 20 cycles (potential range: 1.1-0.05 V, scanning rate: 0.5 V/s) on Pt ring before LSV measurement. For the chronoamperometry measurement, the potential was fixed at 0.25 V (vs. RHE). The collection efficiency (N) on the RRDE electrode was determined in 1 M KCl +10 mM $K_3[Fe(CN)_6]$ at different rotate speeds, in which the potential on disk was scanned from 0.5 V to -0.2 V (vs. Ag/AgCl) to reduce Fe^{3+} to Fe^{2+} while the potential on Pt ring was held at 0.5 V (vs. Ag/AgCl) to oxidize Fe^{2+} to Fe^{3+} [2]. Thus, the collection efficiency (N) was determined to be 33.4% (Figure S22). All the potentials were compensated by

solution resistance and were converted to the reversible hydrogen electrode (RHE). The 0.1 M $HClO_4$ containing 1 mM KSCN and 10 mM H_2O_2 was used as the electrolyte for the poisoning test and H_2O_2 reduction reaction measurements, respectively.

The H_2O_2 selectivity and the transfer number electron (n) were calculated based on the disk current (I_D) and ring current (I_{Ring}) data as the following formulas:

$$H_2O_2\% = 200\frac{I_{Ring}/N}{I_D+I_{Ring}/N} \quad (1)$$

$$n = 4\frac{I_D}{I_D+I_{Ring}/N} \quad (2)$$

The Tafel plots were calculated according to the diffusion-corrected kinetic current density (J_k), which was determined through the Koutecky-Levich diffusion formulas as follows:

$$\frac{1}{J} = \frac{1}{J_k} + \frac{1}{J_d} \quad (3)$$

$$\frac{1}{J_d} = \frac{1}{0.62nFC_0D_{O_2}^{2/3}\upsilon^{-1/6}\omega^{1/2}} \quad (4)$$

In equation (3), J refers to the experimental current density, J_k is the kinetic current density, and J_d indicates the limiting diffusion current density. In equation (4), n is the total transfer electron number, F indicates the Faraday constant (96485 C mol^{-1}), C_0 represents saturated O_2 concentration in 0.1 M $HClO_4$ (1.26×10^{-3} mol L^{-1}), D_{02} refers to the diffusion coefficient of O_2 (1.93×10^{-5} cm^2 s^{-1}), υ indicates the kinetic viscosity of the electrolyte (0.01 cm^2 s^{-1}), ω is the rotation speed (rad·s^{-1}) of RRDE electrode.

***In situ* attenuated total reflectance surface-enhanced infrared absorption spectroscopy (ATR-SEIRAS) measurements.** *In situ* ATR-SEIRAS was measured on a Nicolet iS50 FT-IR spectrometer equipped with an MCT detector which was cooled by liquid nitrogen in the test process. The electrochemical measurement was carried out in the custom-made three-electrode electrochemical single cell, in which the Ag/AgCl and a Pt wire were employed as the reference and counter electrode, respectively. A Si semi-cylindrical prism (diameter: 20 mm) coated with Au thin layer was used to load catalysts and employed as the working electrode. *In situ* ATR-SEIRAS spectra with a spectral resolution of 4 cm^{-1} were acquired through stepwise varying the potential from 0.9 V to 0.1 V (vs. RHE) in O_2-saturated 0.1 M $HClO_4$. The spectrum obtained at open-circuit voltage was used for the background subtraction.

H_2O_2 yield in the flow cell. The electro-synthesis of H_2O_2 through ORR was carried out using a flow cell setup in a two-compartment cell separated by Nafion membrane. The ink of Co-N SAC_{Dp} catalyst was dropped on the carbon paper (actual working area: 1 cm^2, catalyst loading: 1 mg cm^{-2}) and was assembled into the gas diffusion layer (GDL, SGL29BC) to acquire the cathode. The Ag/AgCl electrode and IrO_2–coating titanium sheet were employed as the reference electrode and anode, respectively. In the flow cell test, the electrolyte (0.1 M $HClO_4$, 100 ml) was recycled across each compartment at the flow speed of 12 mL min^{-1} and the O_2 supply rate was maintained at 20 mL min^{-1} flowing through the cathode. For the test of H_2O_2 production rate and stable H_2O_2 production, the cathode current was maintained at -50 mA. The 0.1 M $HClO_4$ electrolyte was refreshed periodically at every 30 h in the stable H_2O_2

production up to 90 h.

The faradaic efficiency of the H_2O_2 production ($FE_{H_2O_2}$) was determined by the following formula:

$$FE_{H_2O_2}(\%) = 2FCV / Q \quad (5)$$

Where F indicates the faraday constant (96485 C mol^{-1}), C is the produced H_2O_2 concentration (mol L^{-1}) in the electrolyte, V refers to the volume of electrolyte (L), Q represents the consumed charge amount (C). In this chronopotentiometry process, the Q was calculated according to the following formula:

$$Q = It \quad (6)$$

Where I indicates the constant current of -50 mA and the t refers to running time.

The produced H_2O_2 was measured according to the $Ce(SO_4)_2$ titration method. After addition of H_2O_2, the yellow Ce^{4+} turned into colorless Ce^{3+}. The reaction equation and linear relation to determining the $C_{H_2O_2}$ were shown as follows:

$$2Ce^{4+} + H_2O_2 \rightarrow 2Ce^{3+} + 2H^+ + O_2 \quad (7)$$

$$C_{H_2O_2} = 1/2\Delta C_{Ce^{4+}} \quad (8)$$

A linear calibration relationship between Ce^{4+} concentration and the Ce^{4+} absorbance peak at 319 nm was acquired (Figure S39) via using UV-Vis spectroscopy. Thus, the produced H_2O_2 in the electrolyte can be measured referring to the changed Ce^{4+} concentration after the addition of the collected aliquots of electrolyte at a given time.

Electro-Fenton Process for CBZ degradation. The working electrode was prepared as follows. Firstly, 0.05 g catalyst was added into the ethanol/water mixing solution (ethanol: 1 mL, deionized water: 1.5 mL) containing 0.15 mL polytetrafluorethylene (PTFE), and then the homogeneous catalyst ink was coated on graphite felt (GF, area: 2 cm×1 cm). Then, the GF coated with catalyst was calcined at 360 ºC for 30 min and the working electrode was obtained.

The obtained work electrode was used as the cathode, and platinum electrode (1×1 cm^2) was chosen as the anode in which the distance between the anode and cathode was fixed at 1 cm. The 0.05 M Na_2SO_4 (0.1 L) solution containing 0.4 mM $FeSO_4$ was employed as electrolyte solution accompanied with 0.7 min/L air aeration. The initial CBZ concentration is 10 mg L^{-1}, and the pH of the electrolyte is adjusted to 3 by adding H_2SO_4.

In the degradation process, 1 mL of the electrolyte solution was extracted at a given time and then filtered into a vial for the next analysis. The high-performance liquid chromatography (HPLC, Shimadzu, LC-16) equipped with an Agilent SB–C18 column (2.1 mm×100 mm, 1.8 μm) was employed to measure the CBZ concentration. The mobile phase is composed of acetonitrile (30%) and water (70%, containing 0.10% formic acid) with a flow speed of 0.20 mL min^{-1}. The UV detector was fixed at 285 nm.

Computational details. All the first-principles spin-polarized calculations were performed by using plane-wave density functional theory (DFT) as implemented in the Vienna Ab Initio Simulation Package (VASP) [3, 4]. The exchange-correlation potential is treated with the Perdew-Burke- Ernzerhof (PBE) formula by using the projected augmented wave (PAW) method within the generalized gradient approximation (GGA)[5]. The cut-off energy for all calculations is set to be 500 eV. All the positions of

atoms are fully relaxed until the Hellmann-Feynman forces on each atom are less than 0.01 eV/Å. Meanwhile, the Brillouin zone is sampled with (2×2×1) Monkhorst–Pack k-points. The DFT-D3 method proposed by Grimme is applied to depict the van der Waals interactions, which has been shown to accurately describe chemisorption and physisorption properties on layered material. A vacuum region of about 15 Å is employed to decouple the periodic replicas.

To estimate the reaction free energy of intermediates (ΔG) at the catalyst (*) surface in ORR procedure, the following equations were employed:

$\Delta G_{OH^*} = (E_{OH^*} + 0.5\times E_{H2} - E_{H2O} - E_*) + (ZPE_{OH^*} + 0.5\times ZPE_{H2} - ZPE_{H2O} - ZPE_*) - T \times (S_{OH^*} + 0.5\times S_{H2} - S_{H2O} - S_*)$

$\Delta G_{O^*} = (E_{O^*} + E_{H2} - E_{H2O} - E_*) + (ZPE_{O^*} + ZPE_{H2} - ZPE_{H2O} - ZPE_*) - T \times (S_{O^*} + S_{H2} - S_{H2O} - S_*)$

$\Delta G_{OOH^*} = (E_{OOH^*} + 1.5\times E_{H2} - 2\times E_{H2O} - E_*) + (ZPE_{OOH^*} + 1.5\times ZPE_{H2} - 2\times ZPE_{H2O} - ZPE_*) - T \times (S_{OOH^*} + 1.5\times S_{H2} - 2\times S_{H2O} - S_*$

Where E, ZPE, and S are the total energy, zero-point energy, and entropy of intermediates, respectively. The thermal-correction energies for each intermediates at 298.15 K.

Kinetic barriers are obtained using climbing-image nudged elastic band (CI-NEB). Five (5) images are interpolated between the initial (IS) and the final state (FS) to acquire minimum energy path (MEP), and geometry of the transition state (TS). The total energy and force thresholds for geometry optimizations are 1×10^{-5} eV and 0.05 eV $Å^{-1}$, respectively. TSs are determined through frequency analysis to ensure only one imaginary frequency existed, assigned to MEP's unstable mode[6].

Supplementary Figures

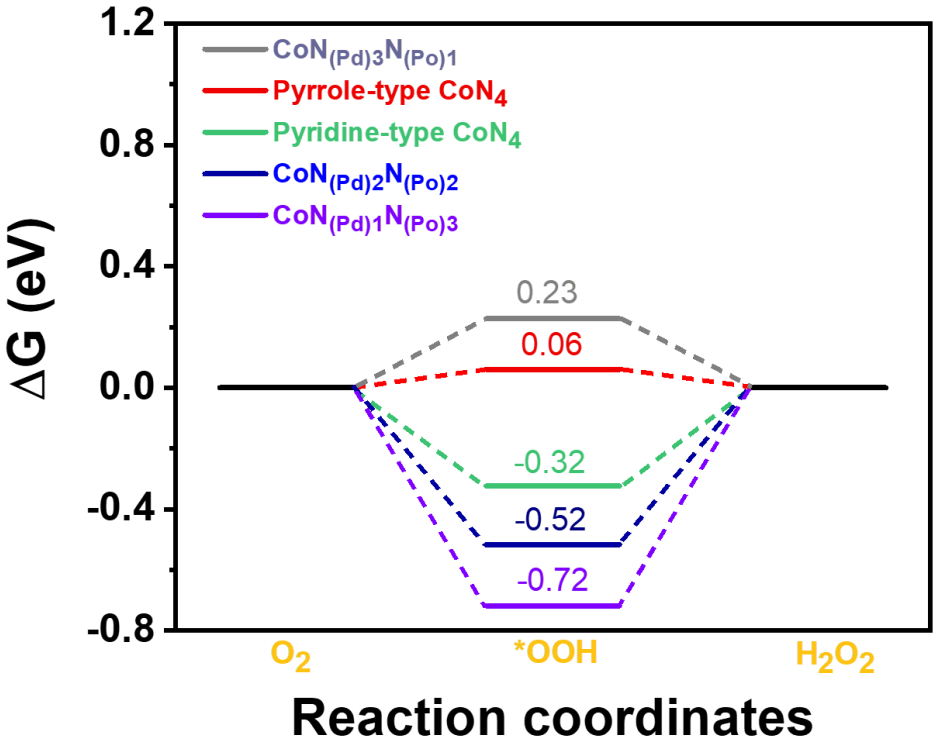

Figure S1. Free energy diagram for H_2O_2 production on the different Co-N coordination structures.

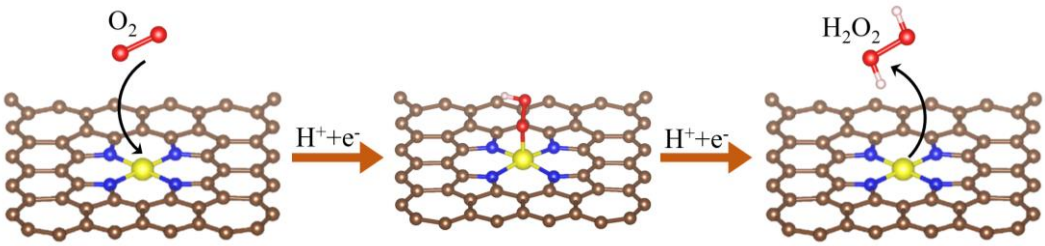

Figure S2. The $2e^-$ ORR pathway and the most stable configurations of reaction intermediates on pyrrole-type CoN_4.

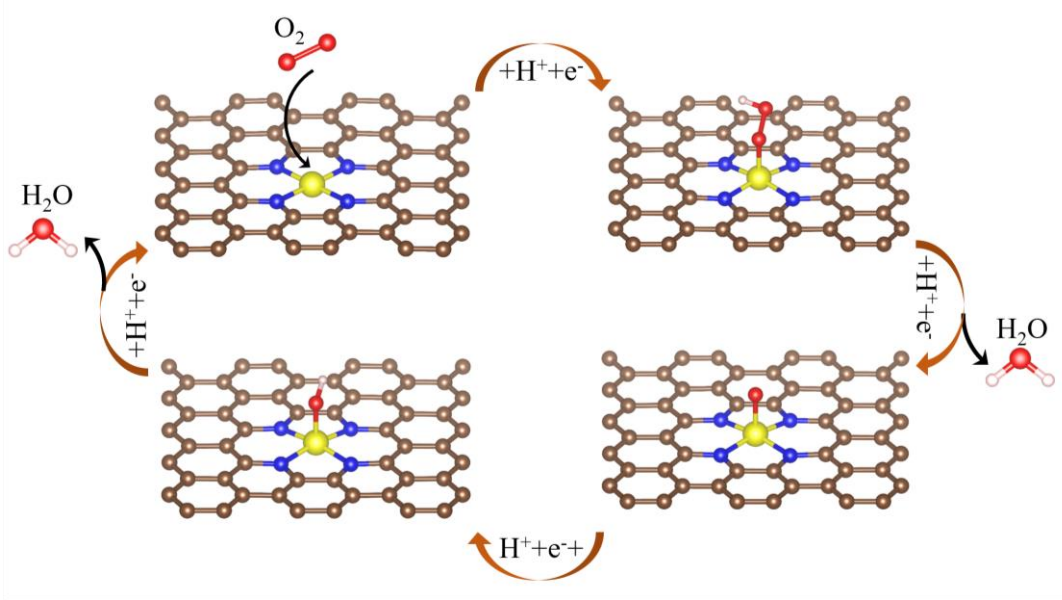

Figure S3. The 4e⁻ ORR pathway and the most stable configurations of reaction intermediates on pyridine-type CoN_4.

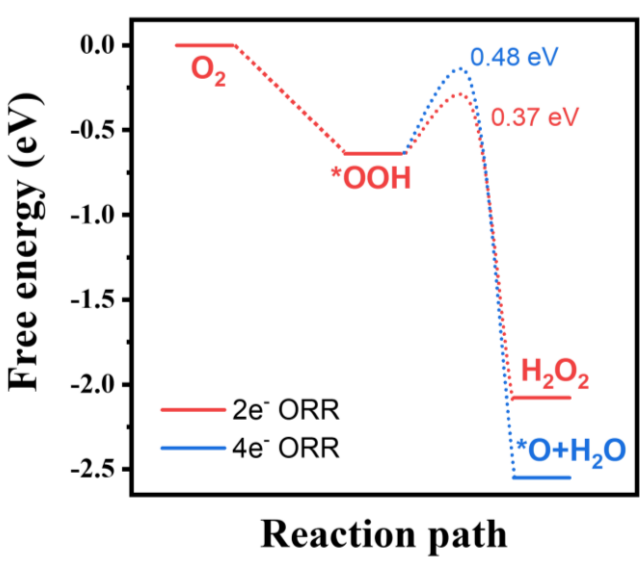

Figure S4. Free energy diagram for $2e^-$ ORR or $4e^-$ ORR on the pyrrole-type CoN_4. The kinetic barriers for *OOH protonation and *OOH dissociation are calculated by the CI-NEB approach.

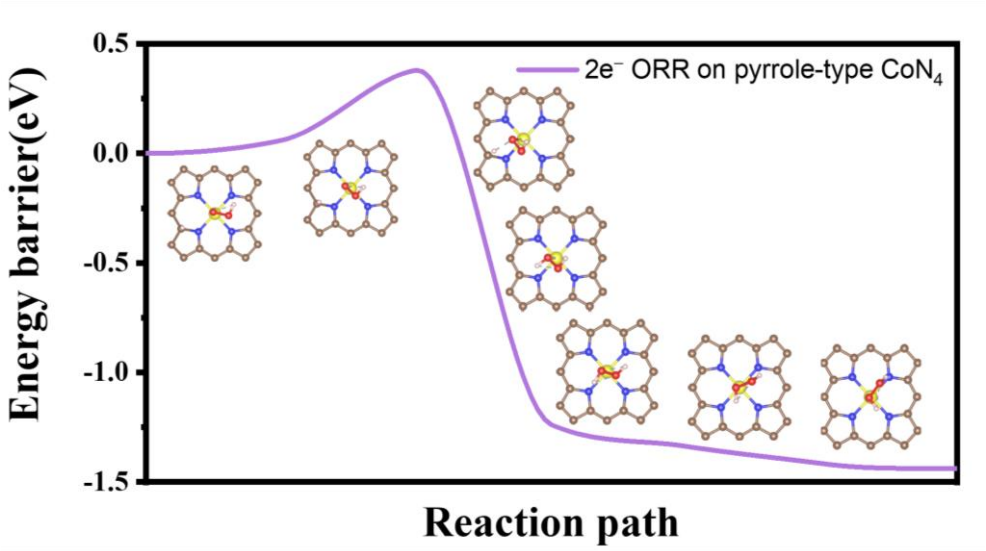

Figure S5. The minimum energy path (MEP) of $2e^-$ ORR on the pyrrole-type CoN_4, Inset: the optimized geometry structures of initial, transition and ultimate states.

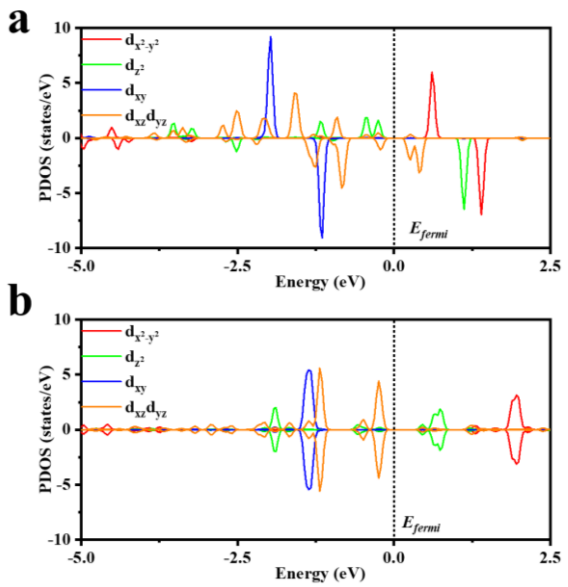

Figure S6. (a) DOS of Co in pyrrole-type Co-N_4 with adsorption of *OOH. (b) DOS of Co in pyridine-type Co-N_4 with adsorption of *OOH.

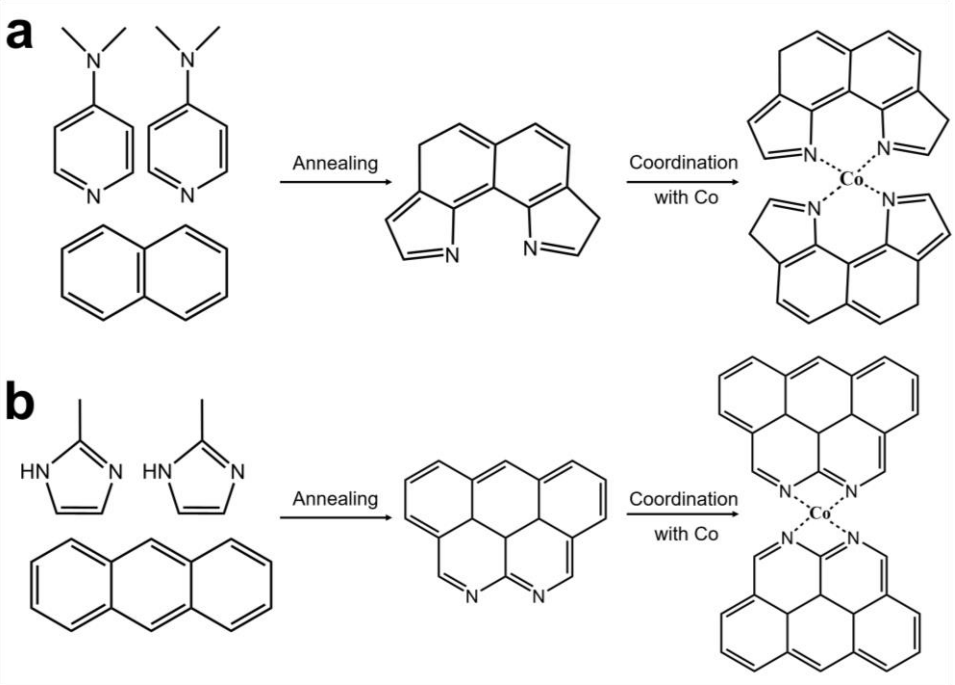

Figure S7. The proposed formation process of (a) pyrrole -type CoN_4 and (b) pyridine -type CoN_4.

The 2-methylimidazole as the typical nitrogen precursor can be used to synthesize the zeolitic imidazolate framework (ZIF) materials. Recently, pyrolysis of Co-based ZIF has been demonstrated as an accurate method to prepare the pyridinic-N coordinated Co-N_4 evidenced by systematic structure characterizations in previous studies [7-9]. On the other hand, the aminopyridine-based precursor has been reported to synthesize the N-doped carbon with high content of pyrrolic-N [10-12]. As shown in Figure S7, the transform process of 2-methylimidazole to pyridinic-N and 4-dimethylaminopyridine to pyrrolic-N through a ring expansion or a condensation reaction is proposed[13,14]. Therefore, the 2-methylimidazole and 4-dimethylaminopyridine are used to prepare the pyridine-type and pyrrole-type CoN_4, respectively.

The coordination environment between the nitrogen precursor and metal has an important effect on the formed M-N-C structure from pyrolysis. Through analyzing the general preparation process of M-N-C, Tim-Patrick Fellinger et al.[15] revealed that the carbothermal reduction between the metal and carbon matrix had a great influence on the formation of the M-N-C coordination structure. Wherein, the pyridine-type MN_4 is formed in the case of strong carbothermal reduction while the formation of pyrrole-type MN_4 is related to inadequate carbothermal reduction. Furthermore, the carbothermal reduction heavily depends on the coordination strength between the metal and nitrogen ligand[15]. In our systems, the different coordination abilities with Co between the 2-methylimidazole and 4-dimethylaminopyridine may influence the carbonization process, giving rise to the difference in the coordination structure of CoN_4.

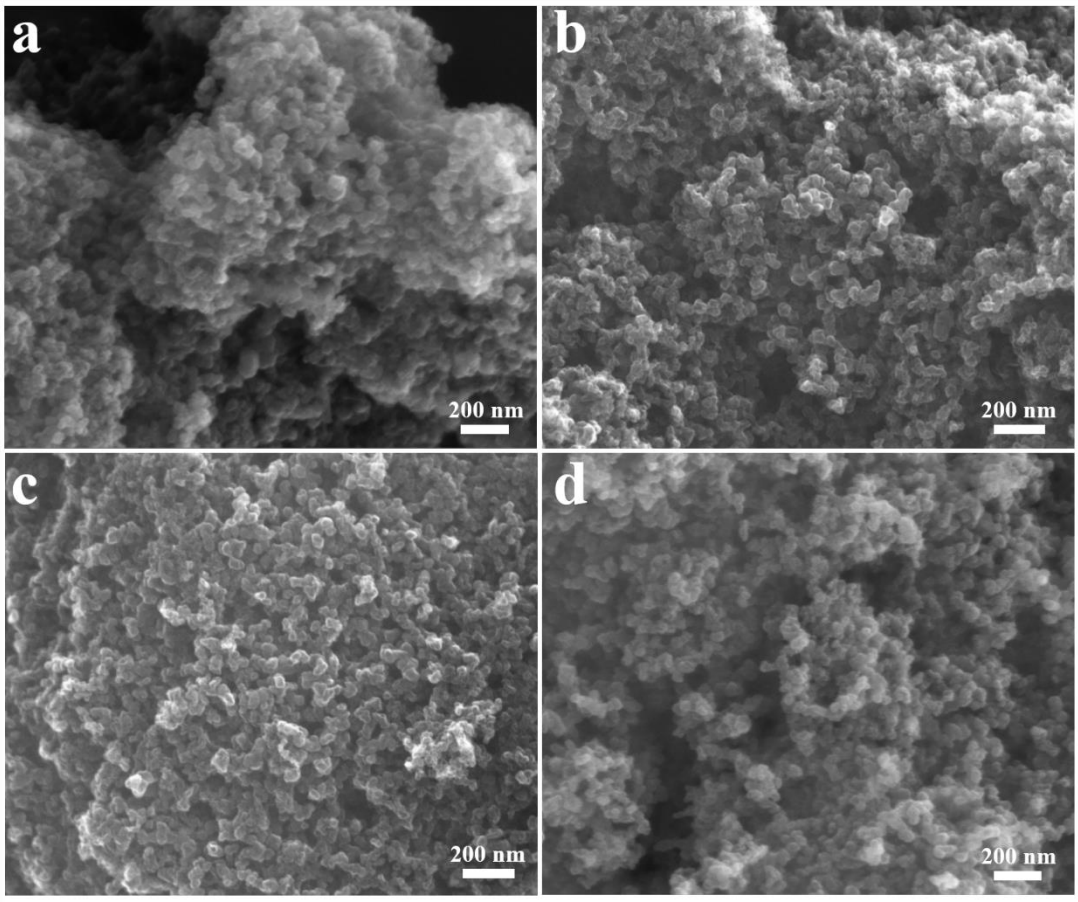

Figure S8. SEM images of (a) carbon black, (b) Co-N SAC_{Dp}, (c) Co-N SAC_{Pc}, (d) Co-N SAC_{Mm}.

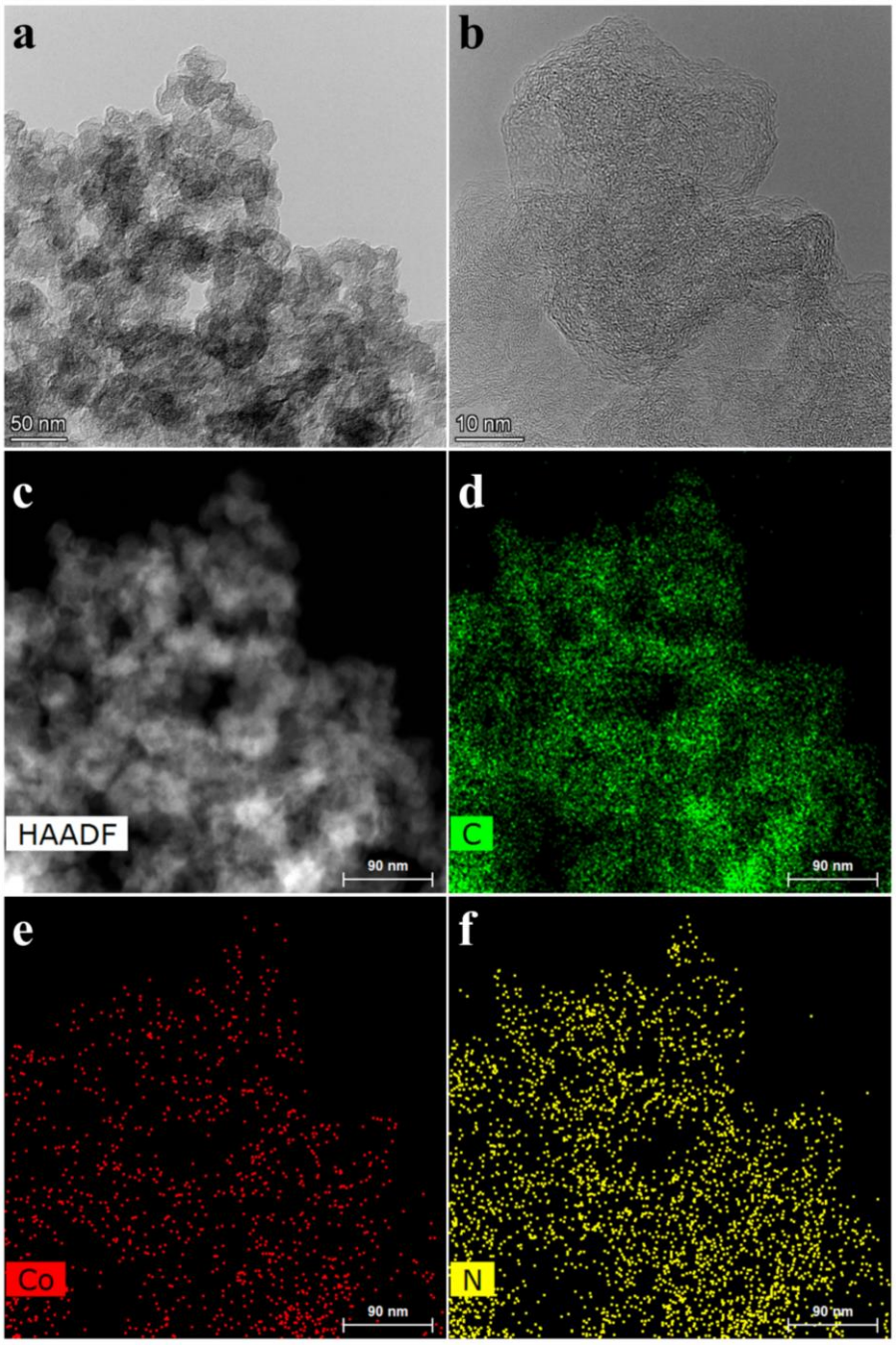

Figure S9. (a-b) TEM images of Co-N SAC_{Pc}. (c) HAADF-STEM images of Co-N SAC_{Pc} (d-f) C, Co, and N element mapping images of Co-N SAC_{Pc}.

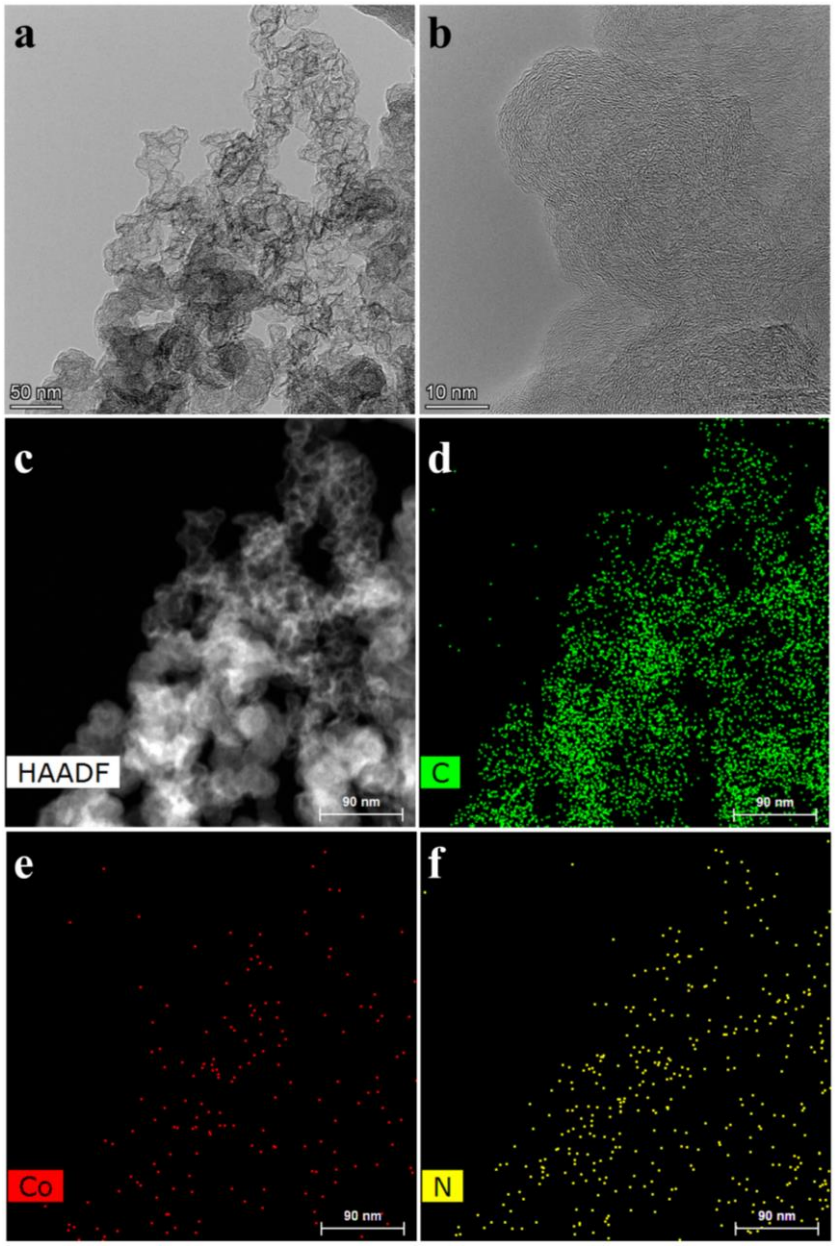

Figure S10. (a-b) TEM images of Co-N SAC_{Mm}. (c) HAADF-STEM images of Co-N SAC_{Mm} (d-f) C, Co, and N element mapping images of Co-N SAC_{Mm}.

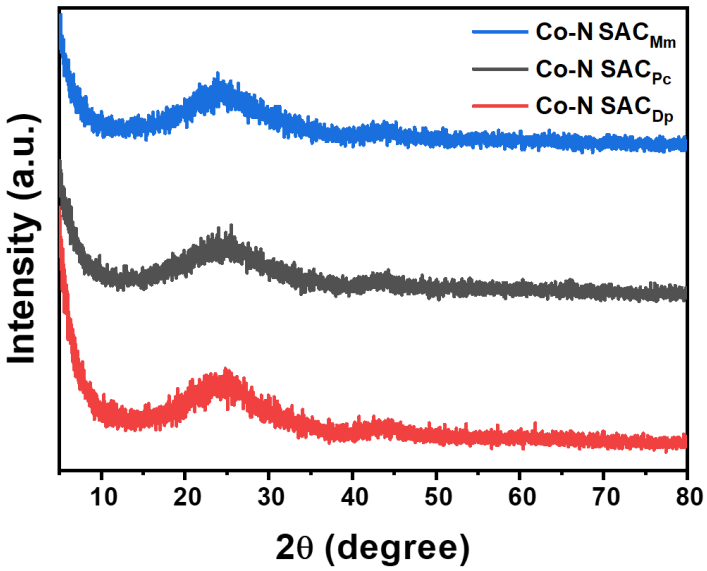

Figure S11. XRD patterns of the different catalysts.

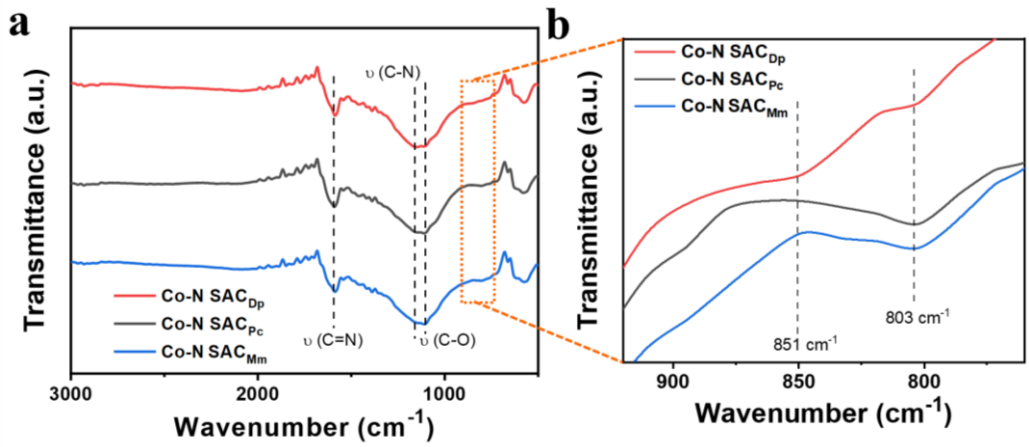

Figure S12. (a-b) FT-IR spectra for Co-N SAC_{Dp}, Co-N SAC_{Pc}, and Co-N SAC_{Mm}.

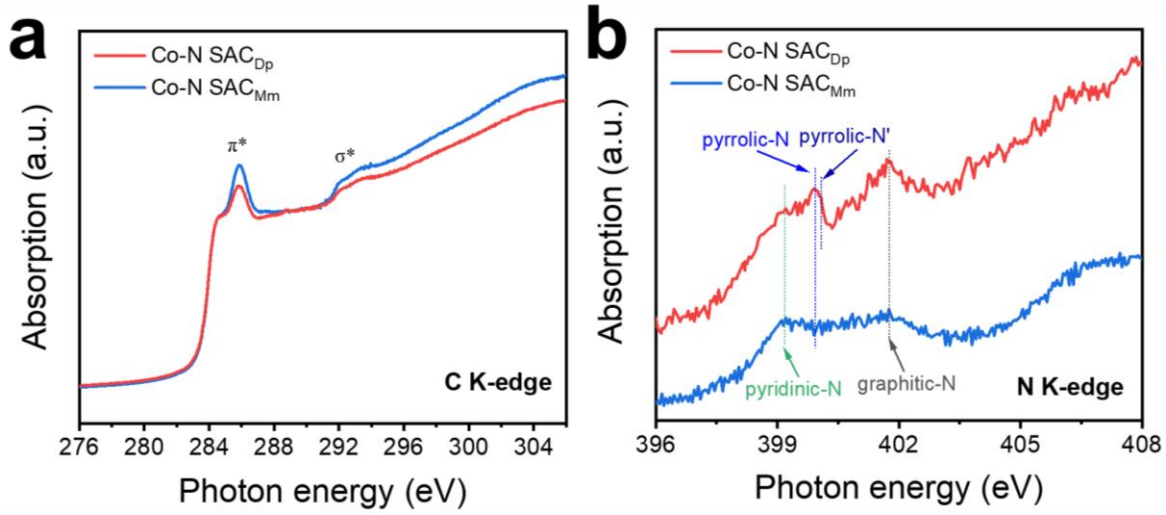

Figure S13. (a) C K-edge and (b) N K-edge spectra of Co-N SAC$_{Dp}$ and Co-N SAC$_{Mm}$.

The C K-edge X-ray absorption near edge structure (XANES) spectra present the π* and σ* resonance (Figure S13), corresponding to 1s core electron of carbon into the $\pi^*_{C=C}$ and σ^*_{C-C} [16], respectively. In the N K-edge XANES spectra, the pyridinic-N (399.1 eV) and graphitic-N (401.8 eV) peaks can be identified for both Co-N SAC$_{Dp}$ and Co-N SAC$_{Mm}$[17]. Notably, the Co-N SAC$_{Dp}$ exhibits the more distinct pyrrolic-N peak (399.9 eV) than that of Co-N SAC$_{Mm}$[17], consistent with the XPS analysis. Furthermore, the splitting pyrrolic-N peak (**pyrrolic-N'**) for Co-N SAC$_{Dp}$ may be ascribed to the metal-pyrrolic N site according to the reported literature[18].

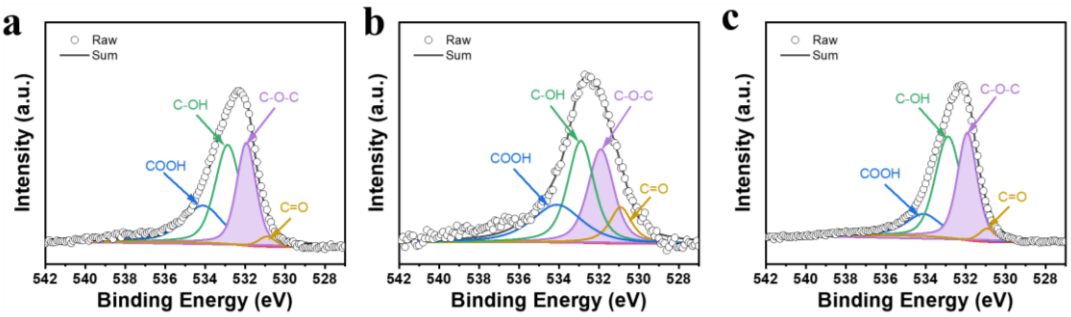

Figure S14. O 1s XPS spectra and the fitted results for (a) Co-N SAC_{Mm}, (b) Co-N SAC_{Dp}, and (c) Co-N SAC_{Pc}.

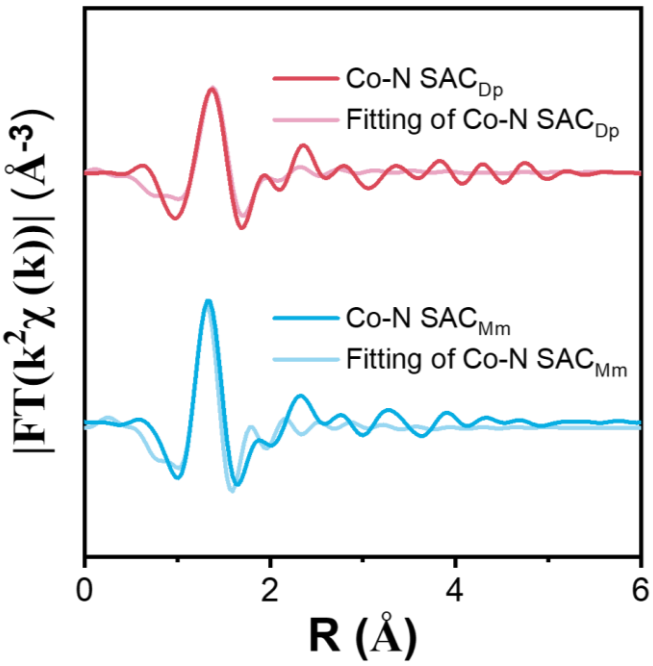

Figure S15. The imaginary part results in the first-shell fitting of EXAFS spectra for Co-N SAC$_{Dp}$ and Co-N SAC$_{Mm}$.

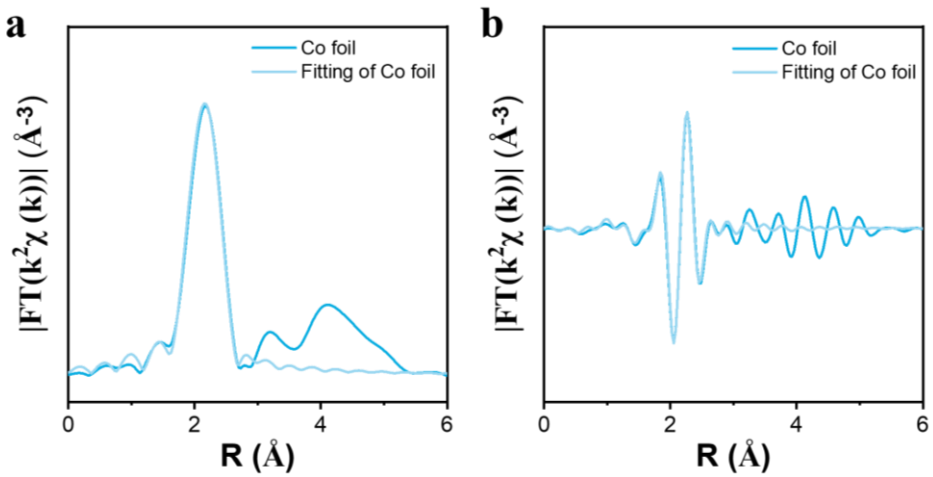

Figure S16. The first-shell fitting of EXAFS spectra for Co-foil. (a) The magnitude part and (b) imaginary part results.

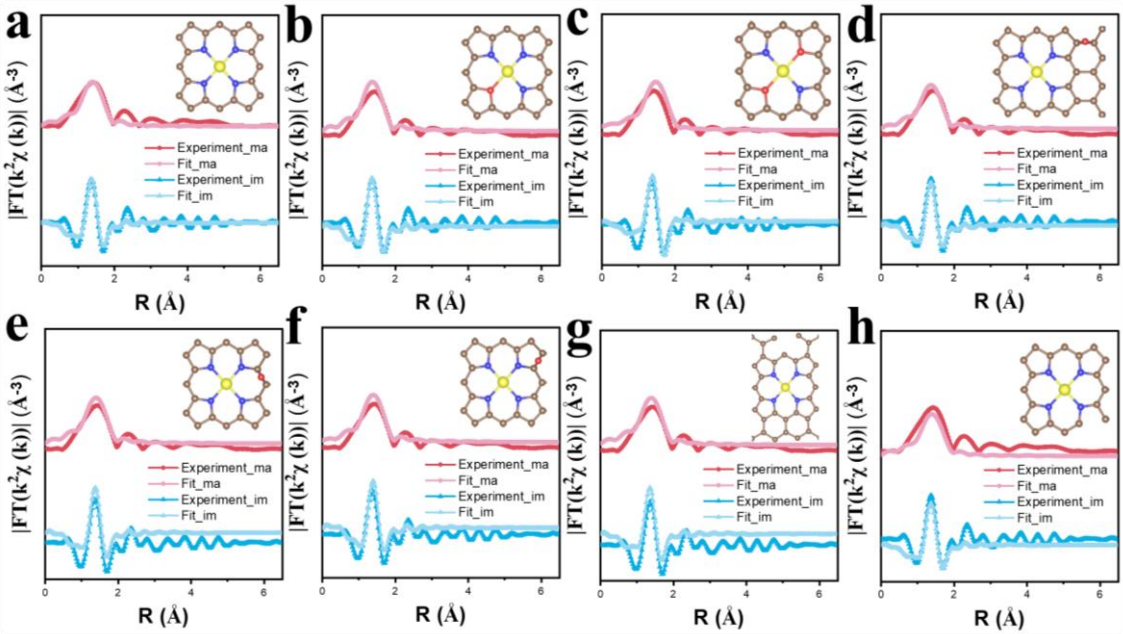

Figure S17. First-shell fitting of FT-EXAFS spectra with different models. (a) Pyrrole-type CoN_4, (b) CoN_3O_1, (c) CoN_2O_2, (d) CoN_4-O_A, (e) CoN_4-O_B, (f) CoN_4-O_C, (g) CoN_4-DF_A, and (h) CoN_4-DF_B. Top and bottom spectra are magnitude and imaginary part, respectively. Inset: The fitting structure.

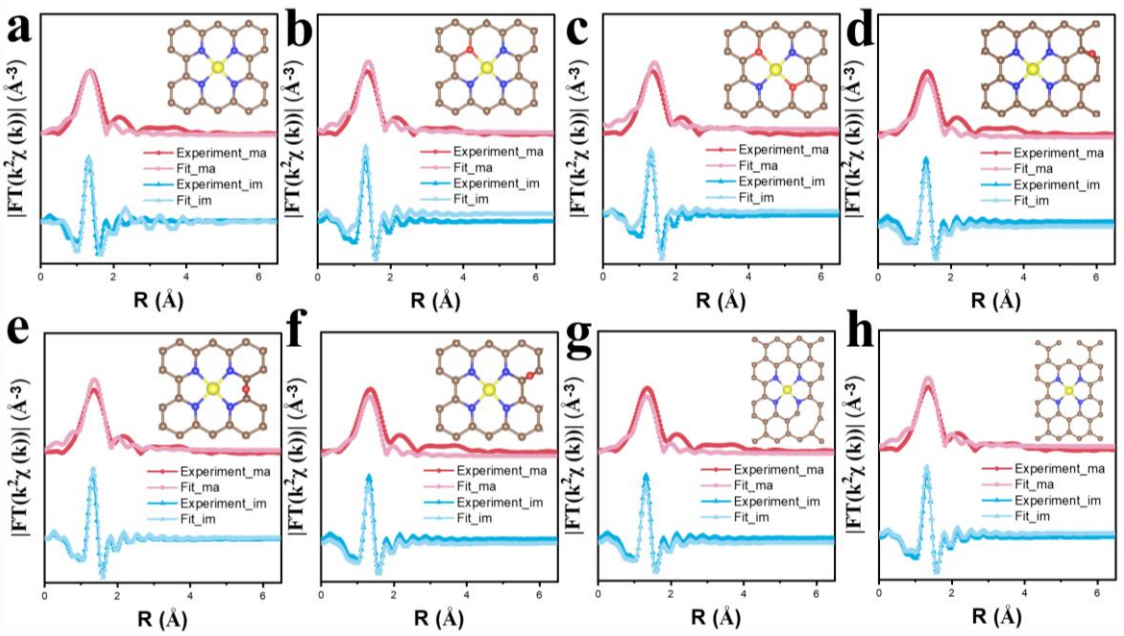

Figure S18. First-shell fitting of FT-EXAFS spectra with different models. (a) Pyridine-type CoN_4, (b) CoN_3O_1, (c) CoN_2O_2, (d) CoN_4-O_A, (e) CoN_4-O_B, (f) CoN_4-O_C, (g) CoN_4-DF_A, and (h) CoN_4-DF_B. Top and bottom spectra are magnitude and imaginary part, respectively. Inset: The fitting structure.

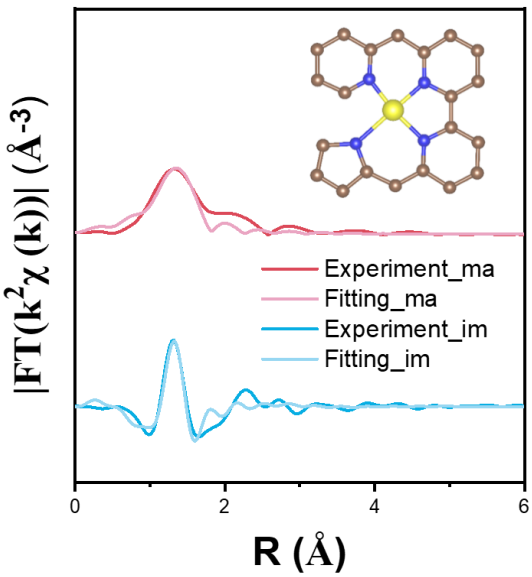

Figure S19. First-shell fitting of Fourier transformations of EXAFS spectra for Co-N SAC_{Pc}. Top and bottom spectra are magnitude and imaginary part, respectively. Inset: The fitting structure.

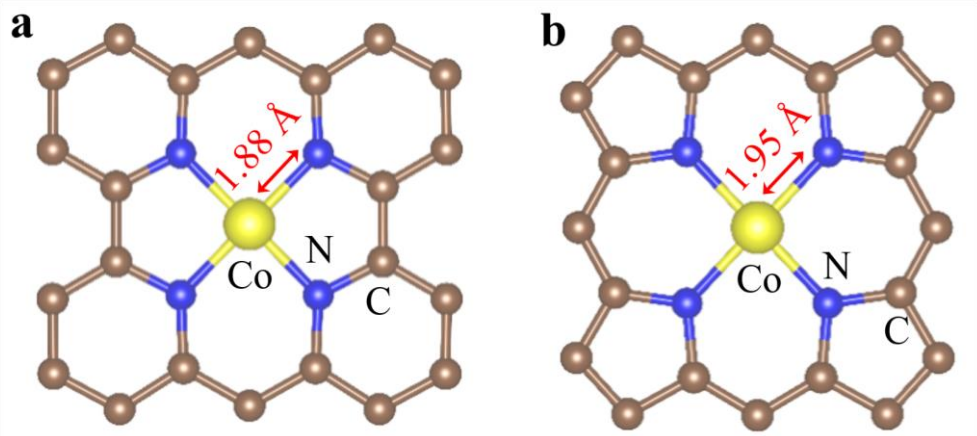

Figure S20. The Co-N length for pyridine-type and pyrrole-type Co-N_4 in DFT calculation.

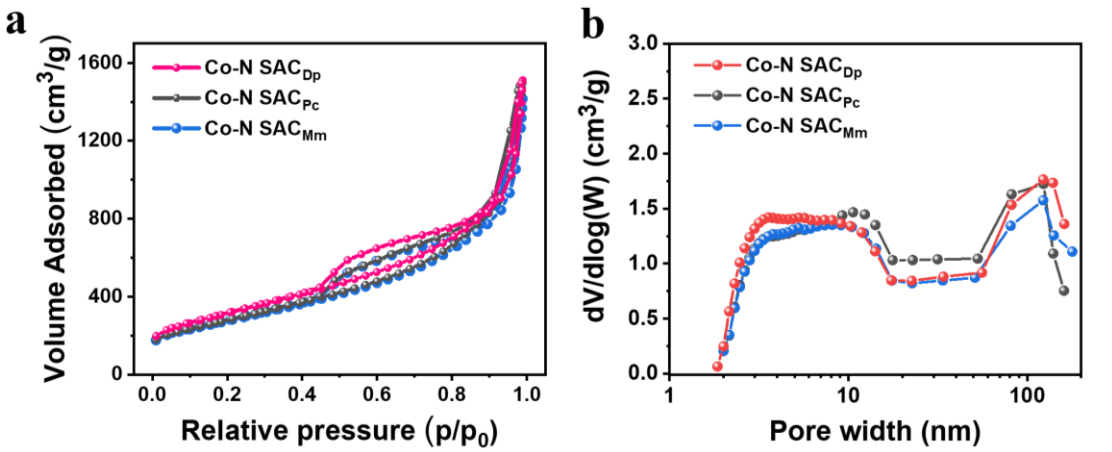

Figure S21. (a) N_2 adsorption/desorption isotherms and (b) pore distribution curves of Co-N SAC_{Dp}, Co-N SAC_{Pc}, and Co-N SAC_{Mm}.

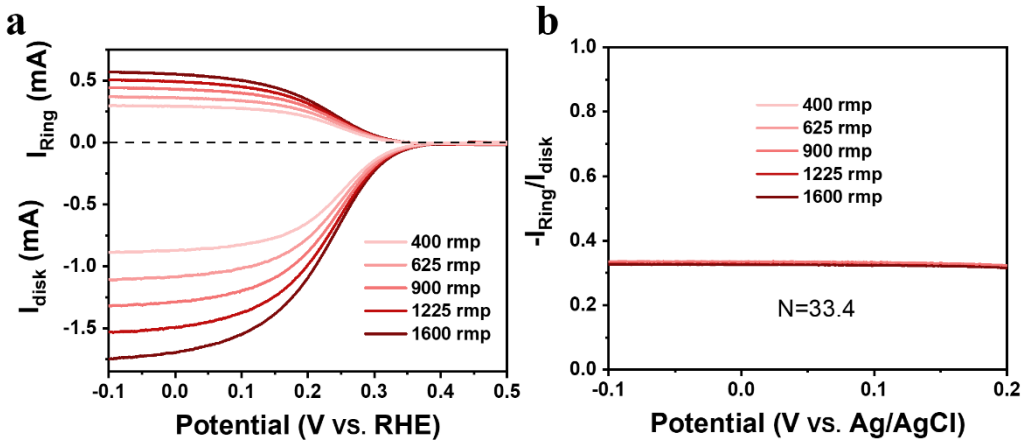

Figure S22. (a) The LSV curves in 1 M KCl +10 mM $K_3[Fe(CN)_6]$ at different rotate speeds. (b) Determination of the collection efficiency (N) for RRDE.

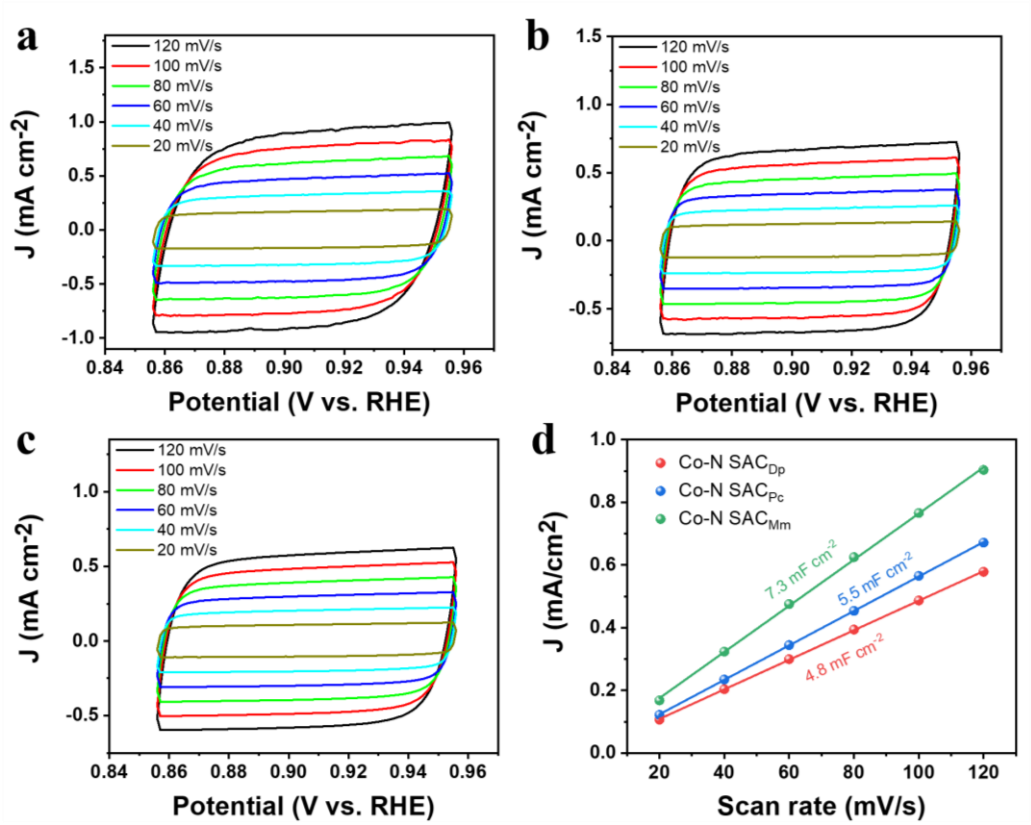

Figure S23. CV curves at different scanning rates of (a) Co-N SAC_{Mm}, (b) Co-N SAC_{Pc}, and (c) Co-N SAC_{Dp}. (d) The calculated ECSA for the three catalysts.

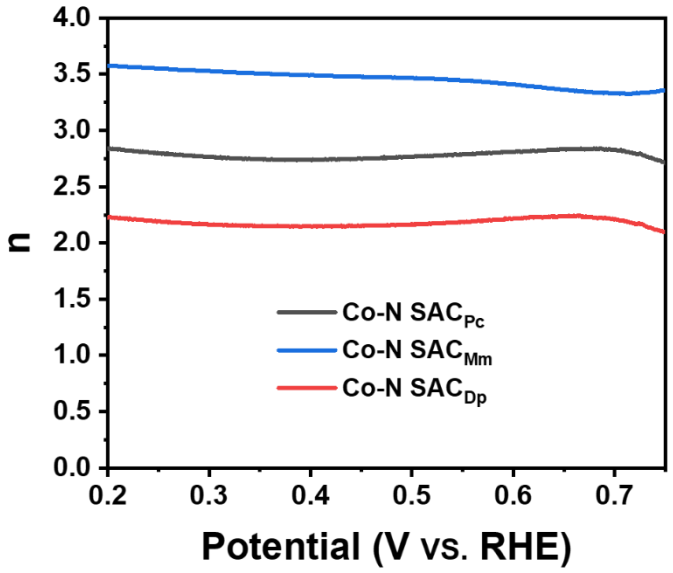

Figure S24. Transfer electron number (n) calculated by formulas (2) for Co-N SAC_{Dp}, Co-N SAC_{Pc}, and Co-N SAC_{Mm}.

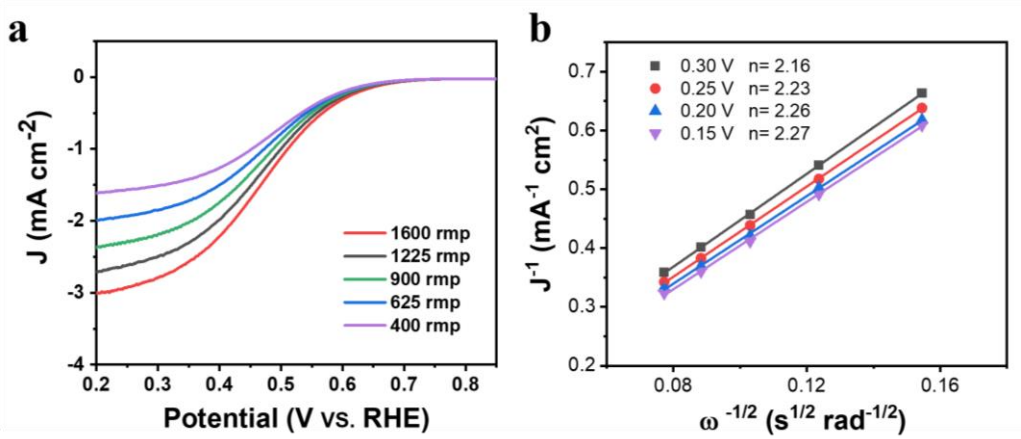

Figure S25. (a) ORR polarization curves of Co-N SAC_{Dp} at different rotate rates. (b) The determined transfer electron number (n) at different potentials based on the Koutecky-Levich diffusion equation (formulas 4).

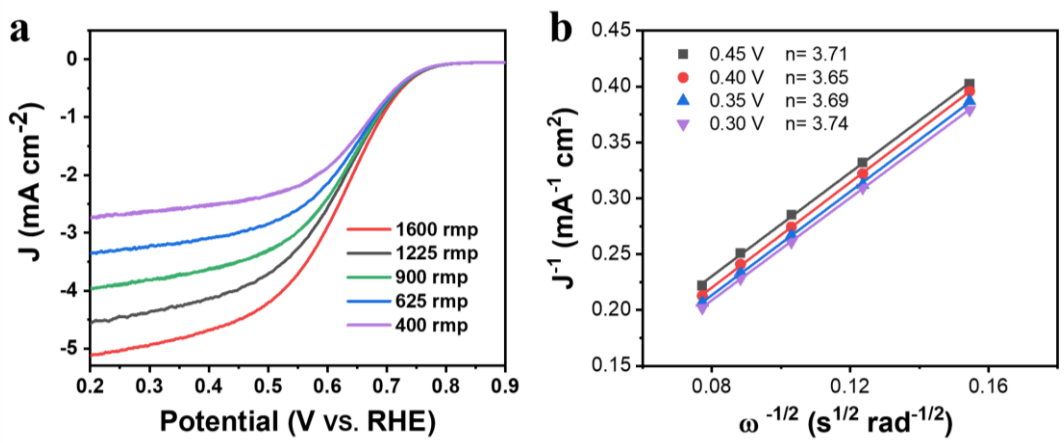

Figure S26. (a) ORR polarization curves of Co-N SAC_{Mm} at different rotate rates. (b) The determined transfer electron number (n) at different potentials based on the Koutecky-Levich diffusion equation (formulas 4).

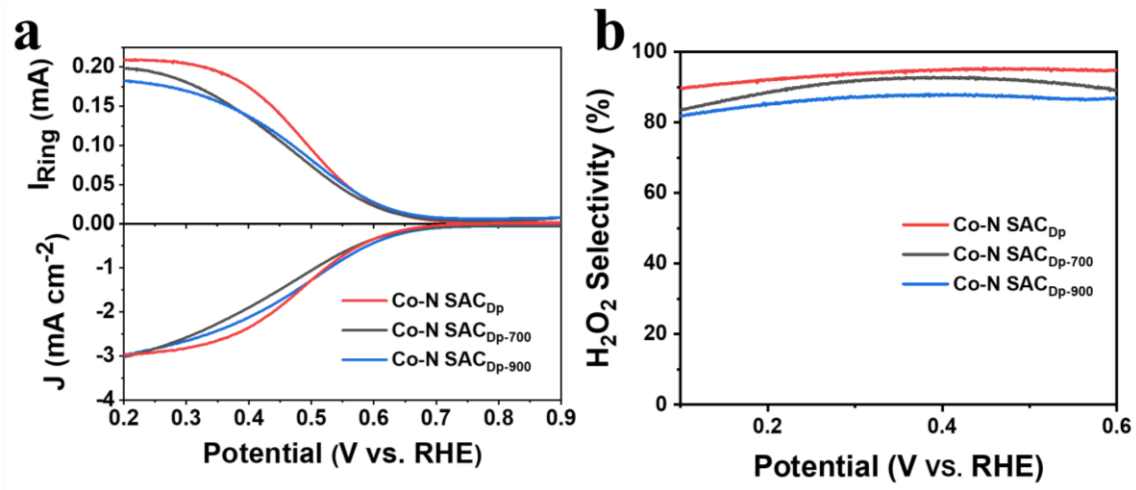

Figure S27. (a) The ORR polarization curves and (b) H_2O_2 selectivity for the Co-N SAC_{Dp} samples pyrolyzed at different temperatures.

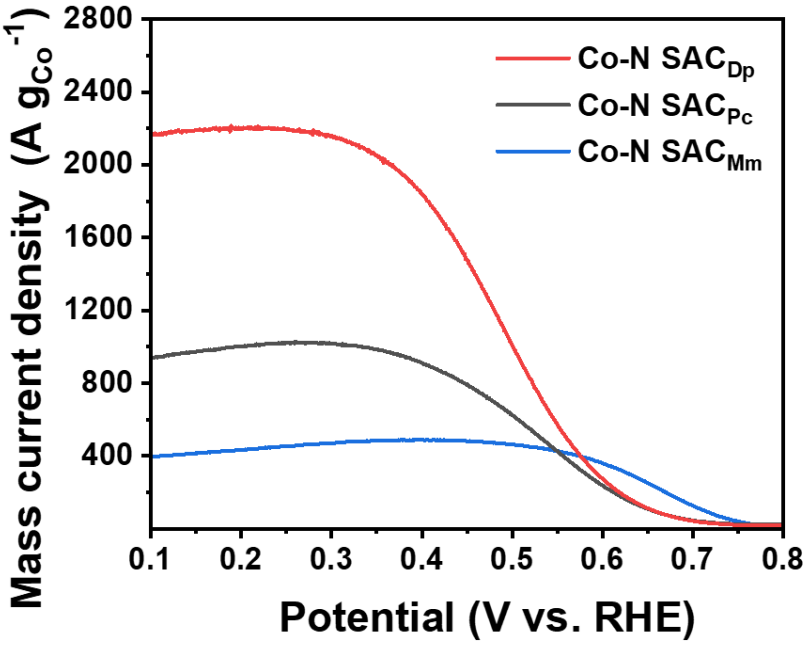

Figure S28. Co mass activity for the three Co-N SAC samples.

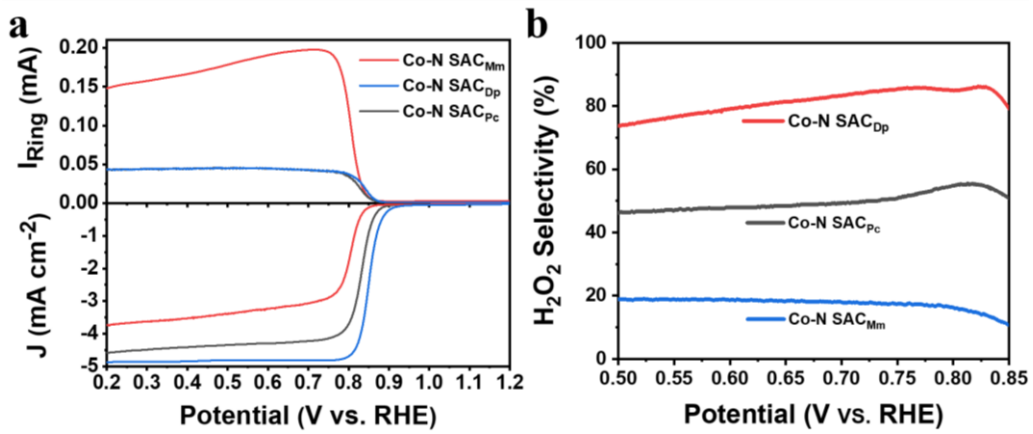

Figure S29. (a) ORR polarization curves and (b) H_2O_2 selectivity of different catalysts in 0.1 M KOH (pH=13).

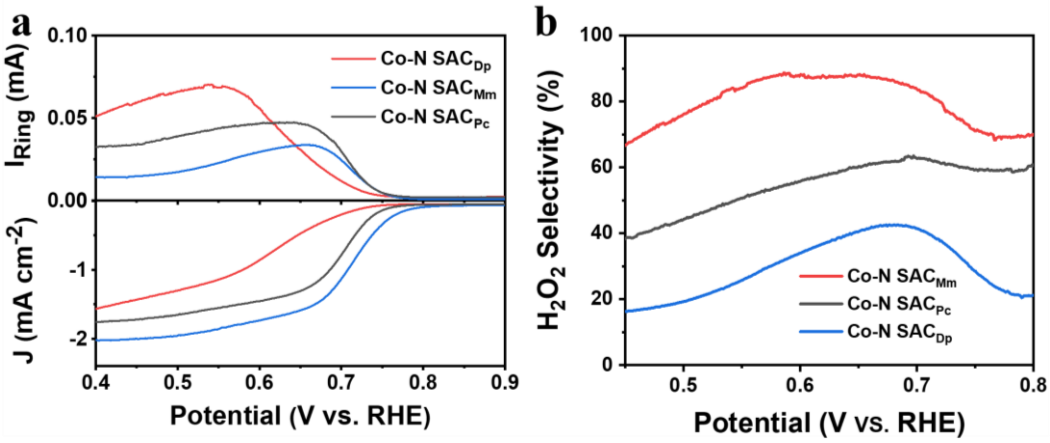

Figure S30. (a) ORR polarization curves and (b) H_2O_2 selectivity of different catalysts in 0.1 M PBS (pH=7.2).

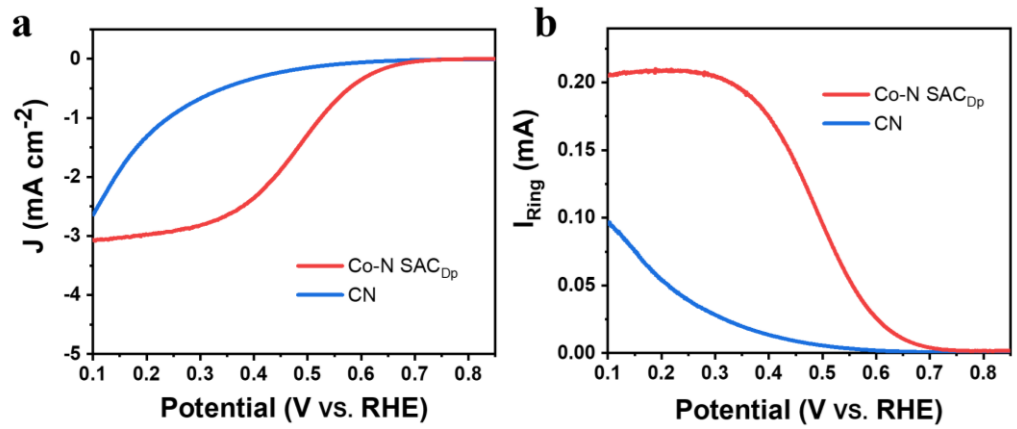

Figure S31. (a-b) ORR polarization curves for CN and Co-N SAC_{Dp}.

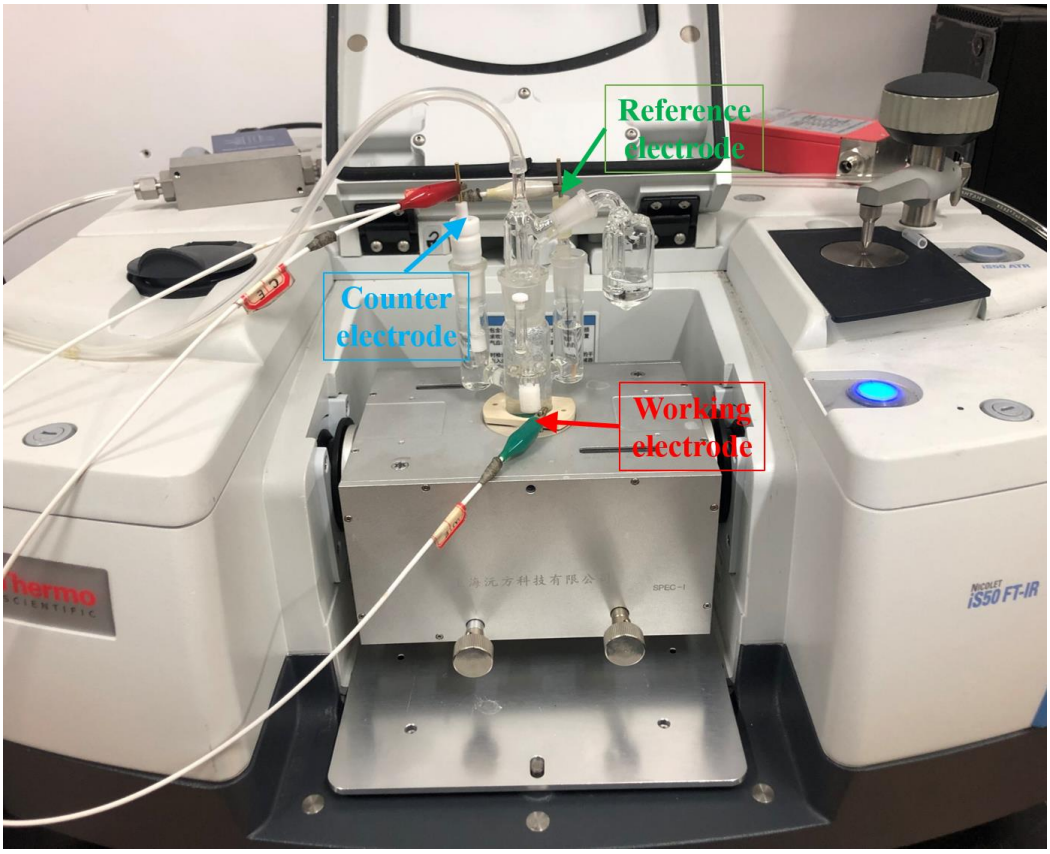

Figure S32. The setup for *in situ* ATR-SEIRAS measurements.

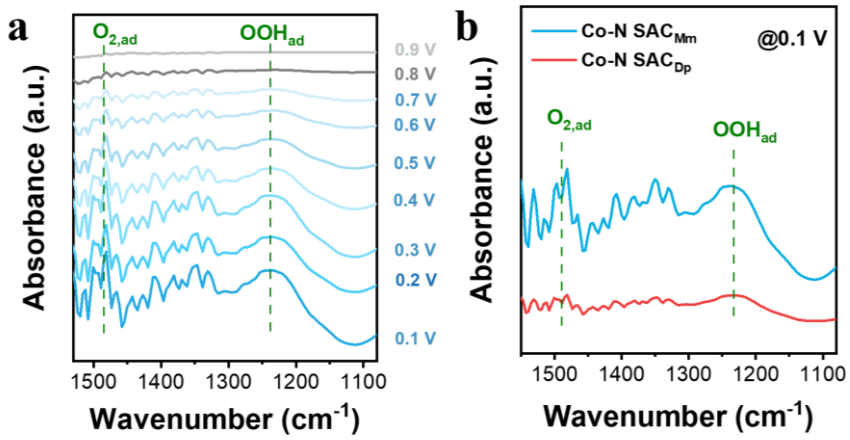

Figure S33. (a) *In situ* ATR-SEIRAS spectra for Co-N SAC_{Mm} at potential range of 0.9 V to 0.1 V. (b) Comparison of *In situ* ATR-SEIRAS spectra for Co-N SAC_{Dp} and Co-N SAC_{Mm} at 0.1 V.

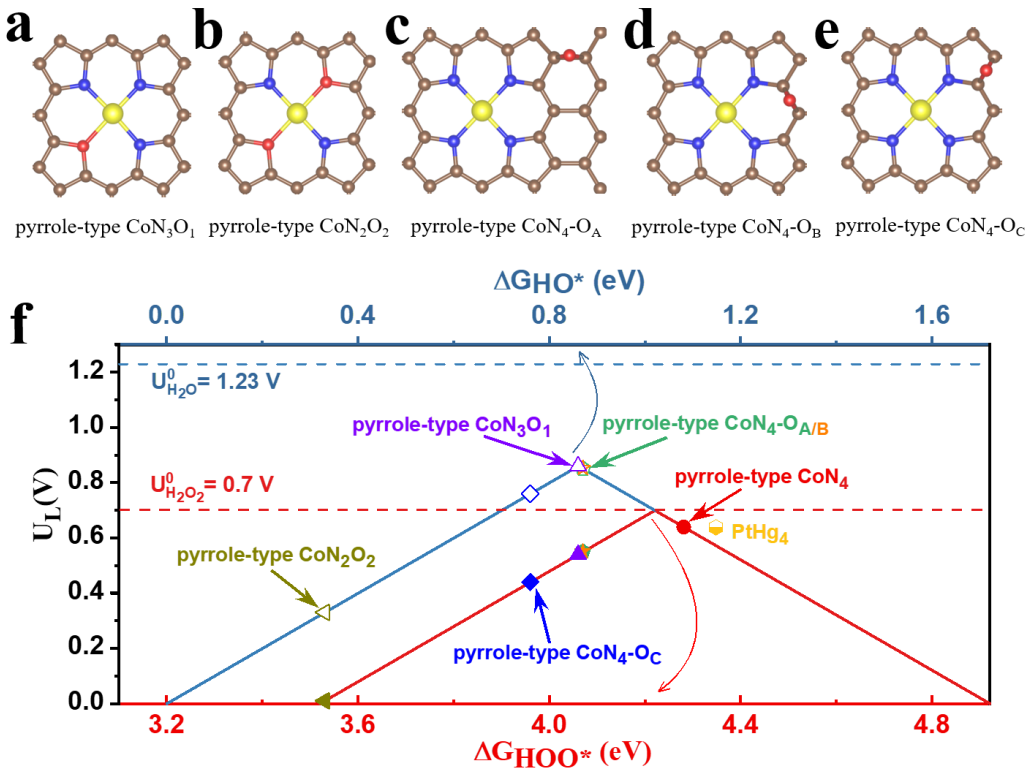

Figure S34. (a-e) The pyrrole-type CoN_4 with C-O-C at different positions. (e) The corresponding volcano plot for Δ_{HO*} and Δ_{HOO*}.

And the introduction of C-O-C in pyrrole-type CoN_4 turns the $2e^-$ ORR into $4e^-$ ORR considering the right shift of Δ_{HOO*} (Figure S34). These theoretical results indicate that the introduction of C-O-C cannot describe the experimental $2e^-$ ORR pathway and high H_2O_2 selectivity for pyrrole-type CoN_4, and the pristine pyrrole-type CoN_4 is more aligned with experimental observation. Noting that the previously reported Co SAC[7, 19, 20] usually is pyridine-type CoN_4, which exhibits the main $4e^-$ ORR pathway. The introduction of C-O-C in pyridine-type CoN_4 can shift the pathway from $4e^-$ ORR to $2e^-$ ORR and thus enhances the H_2O_2 selectivity. However, our pyrrole-type CoN_4 initially shows high H_2O_2 selectivity, and introducing C-O-C will result in lower H_2O_2 selectivity.

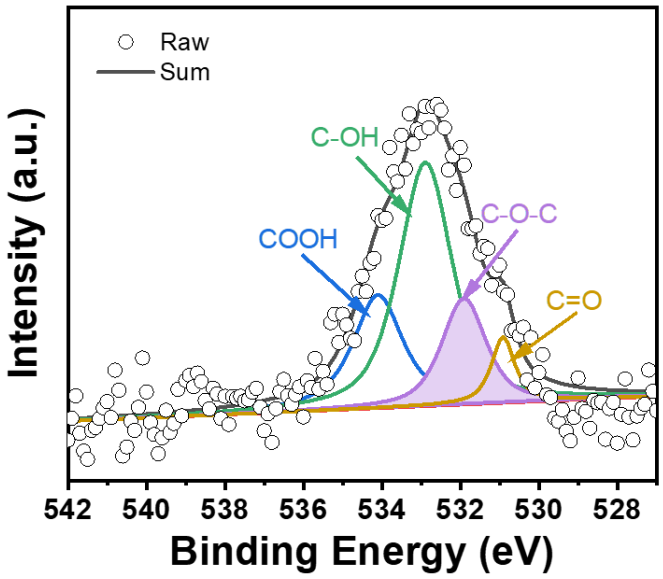

Figure S35. The O 1s XPS spectrum for Co-N SAC_{Dp}-H_2.

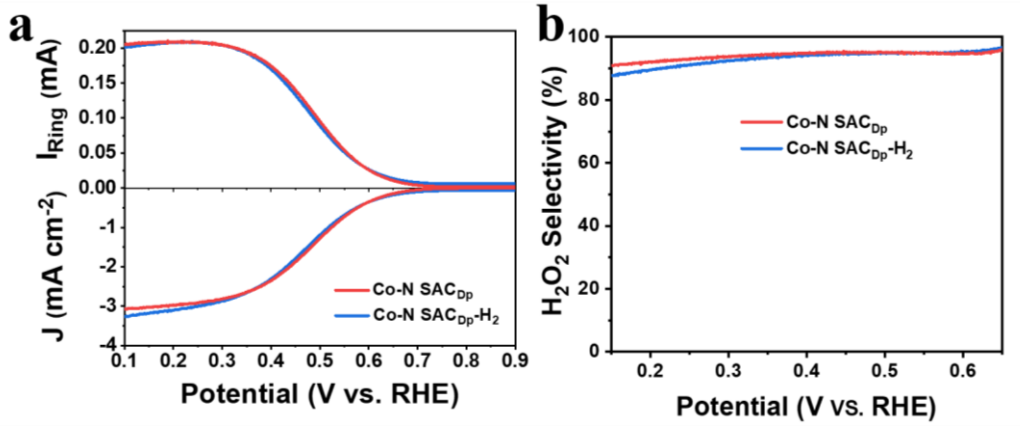

Figure S36. (a) ORR polarization curves of RRDE for Co-N SAC_{Dp} and Co-N SAC_{Dp}-H_2. (b) H_2O_2 selectivity for Co-N SAC_{Dp} and Co-N SAC_{Dp}-H_2.

Compared to the Co-N SAC_{Dp}, the Co-N SAC_{Dp}-H_2 exhibits the significantly decreased oxygen content and C-O-C species (Figure S35 and Table S3), but presents similar H_2O_2 selectivity (Figure S36), indicating the negligible effect of oxygen functional groups on ORR selectivity in our present systems. The experiment results are consistent with the DFT calculation results (Figure S34). Given the results from the experiment investigations and theoretical calculations, we deduce that once the sample is exposed to air, the oxygen functional groups may be formed at the positions of dangling bonds. However, the oxygen functional groups may be far away from the CoN_4 active sites, resulting in very little influence.

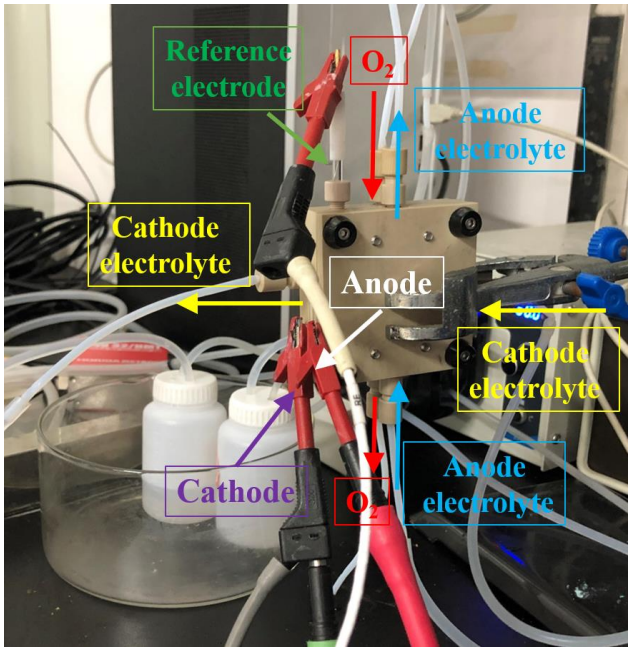

Figure S37. The image of the actually used flow cell setup for H_2O_2 production.

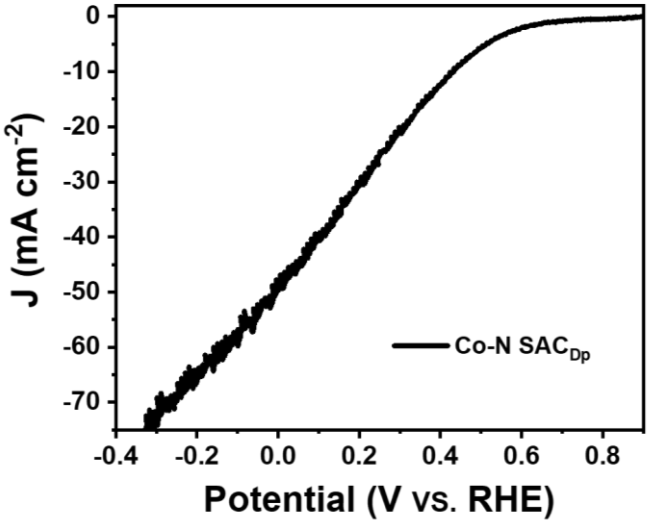

Figure S38. The ORR polarization curve of Co-N SAC_{Dp} in the flow cell.

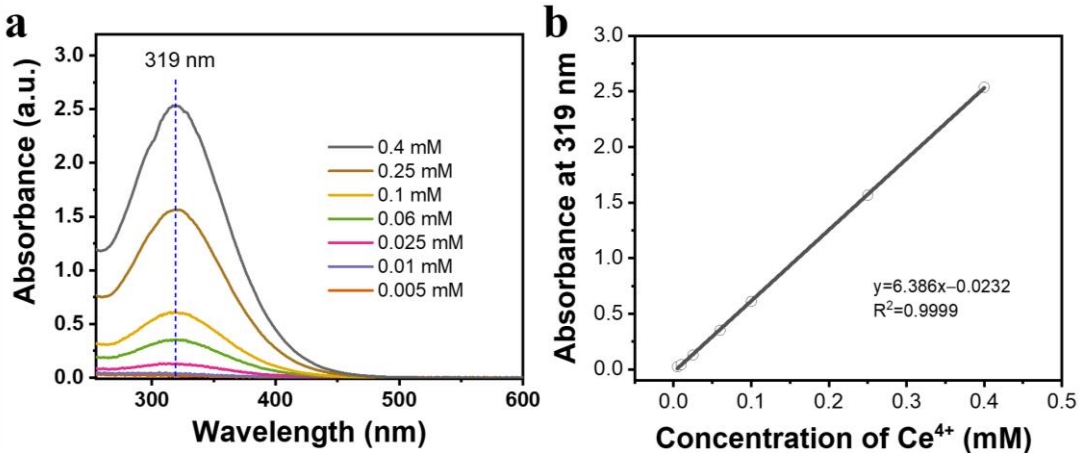

Figure S39. (a) The UV-Vis spectra of Ce^{4+} solutions with different concentrations. (b) The linear calibration relationship between the Ce^{4+} concentration and corresponding absorbance peak at 319 nm.

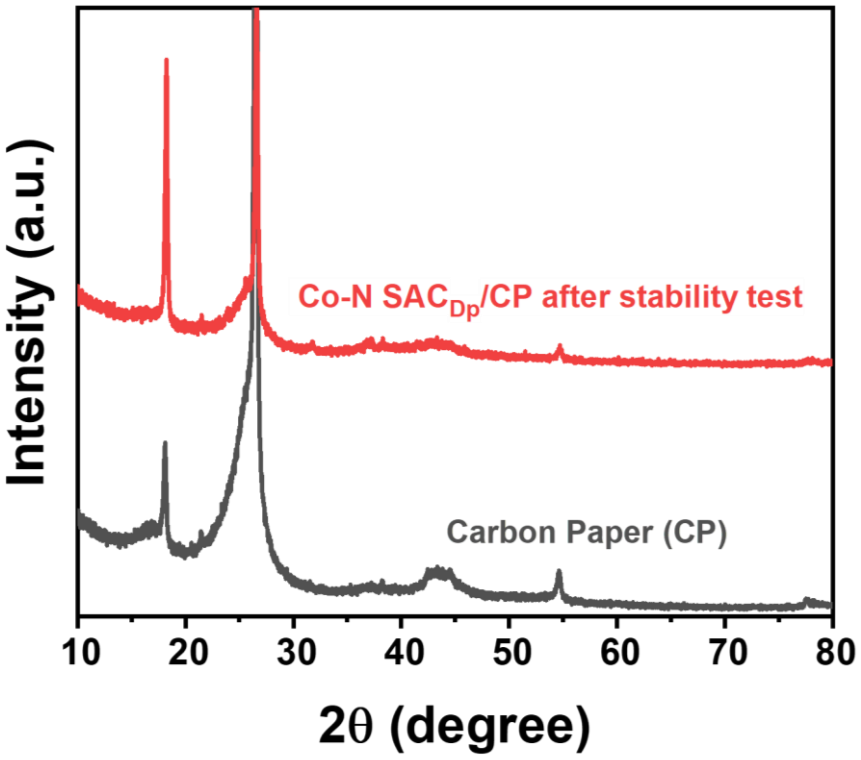

Figure S40. The XRD patterns of the Co-N SAC_{Dp} loading on carbon paper after stability test.

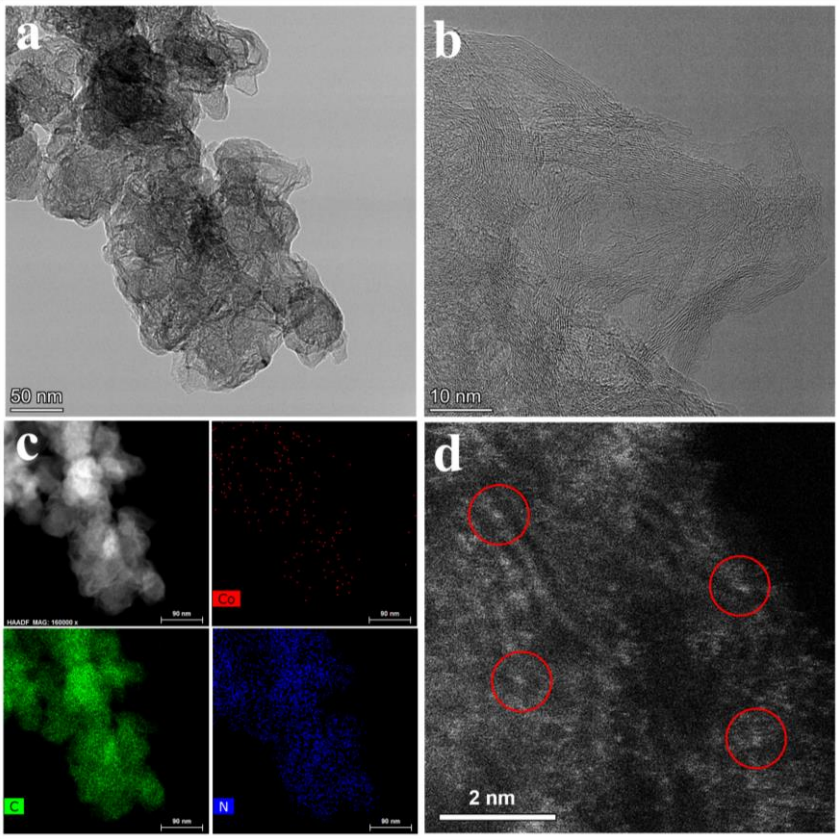

Figure S41. (a-b) TEM, (c) element mapping, and (d) AC-HAADF-STEM images of the used Co-N SAC_{Dp}.

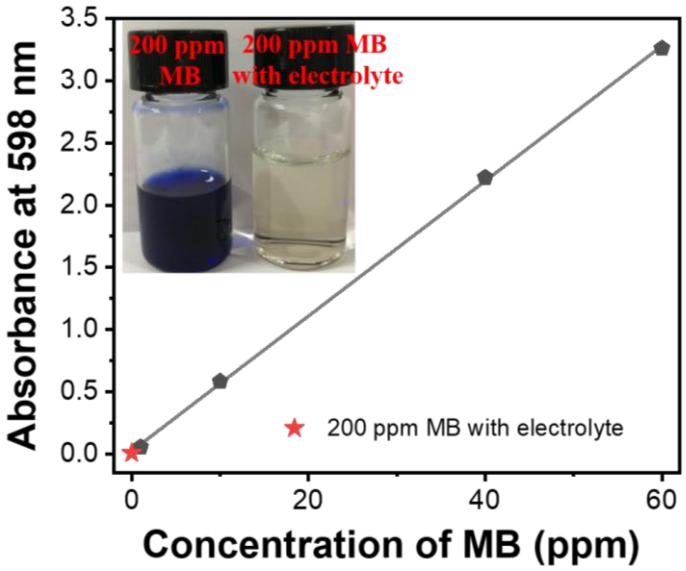

Figure S42. The linear relationship between the MB concentration and absorbance at 598 nm, inset image is the 200 ppm MB (5 mL) before and after addition of electrolyte (2 mL, taken from 30 h).

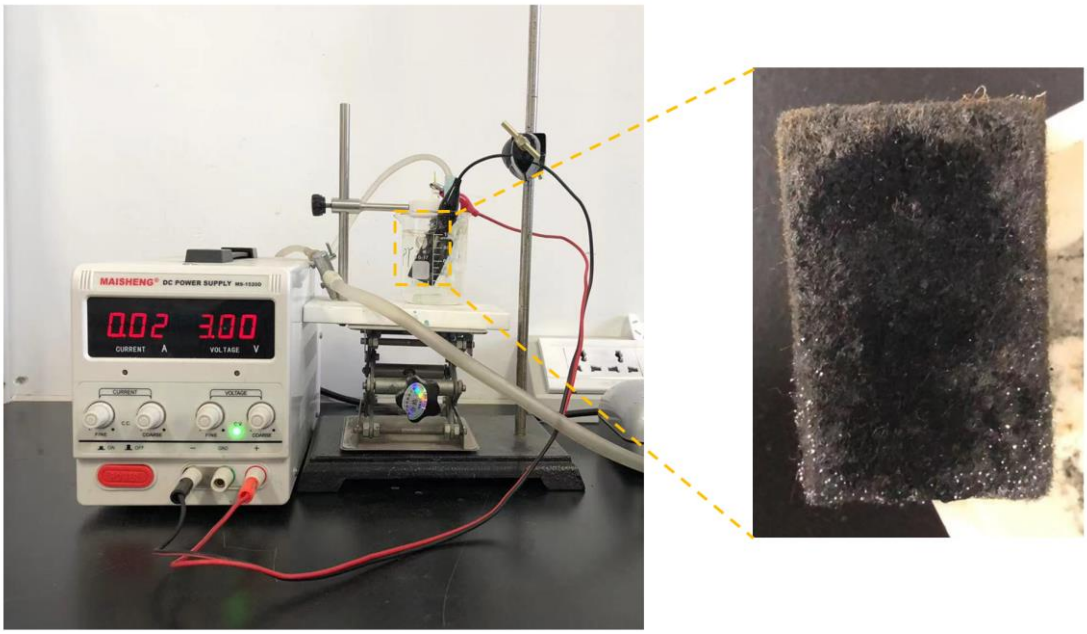

Figure S43. The setup for electro-Fenton degradation of CBZ.

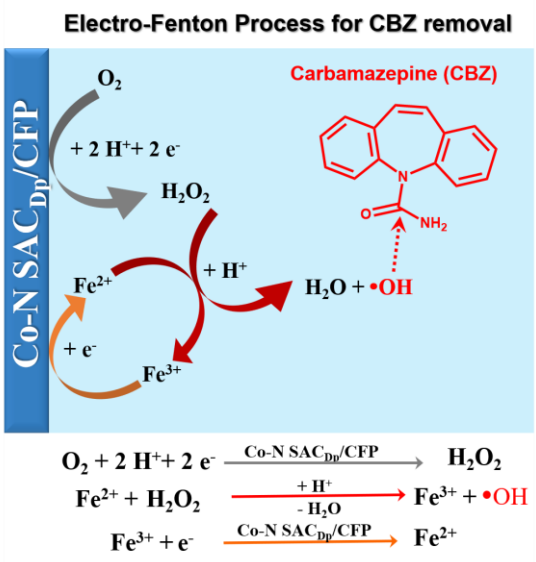

Figure S44. The electro-synthesis of H_2O_2 and electro-Fenton process on Co-N SAC_{Dp} catalyst for CBZ degradation.

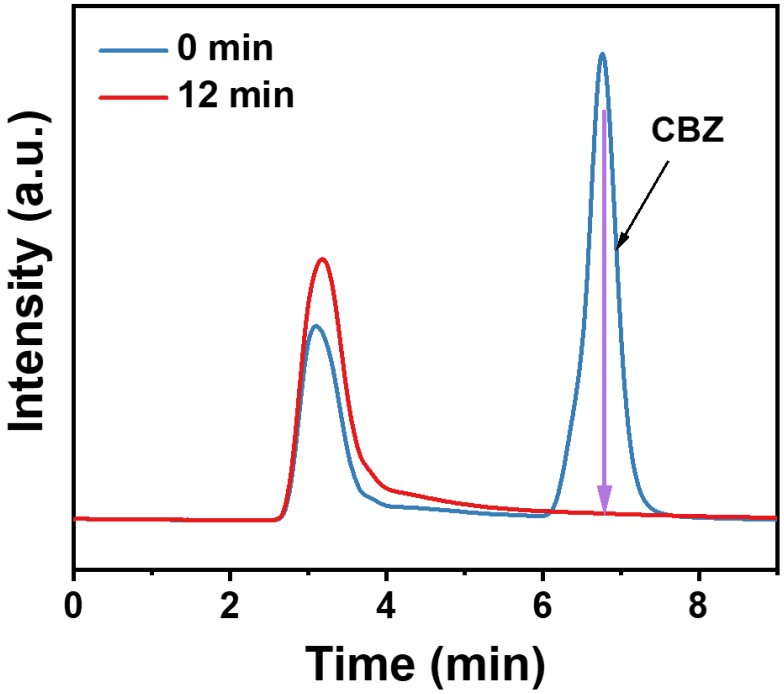

Figure S45. The signal intensity-time curves on HPLC for the CBZ before and after degradation (12 min).

Supplementary Tables

Table S1. Formation energy for different CoN_4 models.

Samples	E_{total} (eV)	E_{sub} (eV)	E_{Co} (eV)	E_F (eV)
Pyridine-type CoN_4	-539.19	-529.61	-7.00	-2.58
$CoN_{(py)3}N_{(po)1}$	-523.00	-515.06	-7.00	-0.94
$CoN_{(py)2}N_{(po)2}$	-506.49	-500.00	-7.00	0.51
$CoN_{(py)1}N_{(po)3}$	-500.78	-491.27	-7.00	-2.52
Pyrrole-type CoN_4	-534.52	-522.91	-7.00	-4.61

The formation energy (E_F) is calculated according to the equation: $E_F = E_{total} – E_{sub} – E_{Co}$, where the E_{total}, E_{sub}, and E_{Co} represent the total energy of the systems, substrate energy, and single Co atom energy in bulk, respectively.

Table S2. The proportion of different nitrogen species for the three catalysts from XPS results.

Samples	Pyrrolic-N (%)	Pyridinic-N (%)	Graphitic-N (%)
Co-N SAC_{Dp}	50.9	28.5	20.6
Co-N SAC_{Pc}	30.6	39.8	29.6
Co-N SAC_{Mm}	14.8	50.0	35.2

The reduced chi-square (χ^2) of N1s XPS fitting is 0.48, 0.56, and 0.73 for Co-N SAC_{Dp}, Co-N SAC_{Pc}, and Co-N SAC_{Mm}.

Table S3. The proportion of different oxygen species for each catalyst from XPS measurements.

Samples	C=O (%)	C-O-C (%)	C-OH (%)	COOH (%)
Co-N SAC_{Dp}	11	31	35	23
Co-N SAC_{Dp}-H_2	7	18	51	24
Co-N SAC_{Pc}	4	37	43	16
Co-N SAC_{Mm}	3	32	40	25

The reduced chi-square (χ^2) of O1s XPS fitting is 0.34, 0.53, 0.79, and 0.42 for Co-N SAC_{Dp}, Co-N SAC_{Dp}-H_2, Co-N SAC_{Pc}, and Co-N SAC_{Mm}.

Table S4. The Co K-edge EXAFS fitting results for Co-N SAC_{Dp} with different models.

Samples	S_0^2	CN	σ^2 (Å^2)	ΔE_0 (eV)	R (Å)	R-factor
pyrrole-type CoN_4	0.71	3.86	0.00923	-1.55	2.02	0.0190
pyrrole-type CoN_3O_1	0.71	3.88	0.00684	-2.87	1.99	0.0295
pyrrole-type CoN_2O_2	0.71	3.87	0.0109	3.54	2.04	0.0423
pyrrole-type CoN_4-O_A	0.71	3.89	0.00889	-2.94	2.00	0.0523
pyrrole-type CoN_4-O_B	0.71	3.88	0.00813	-1.71	2.01	0.0347
pyrrole-type CoN_4-O_C	0.71	3.85	0.00681	-2.87	2.02	0.0313
pyrrole-type CoN_4-DF_A	0.71	3.87	0.00808	-0.744	2.00	0.0361
pyrrole-type CoN_4-DF_B	0.71	3.85	0.00981	-1.49	2.01	0.0282

Screened from different theoretical models (Table S4), considering the small R-factor the pristine pyrrole-type CoN_4 model shows the best fitting goodness for the Co-N SAC_{Dp} sample as compared to the CoN_4 models modified with C-O-C groups or defects.

Table S5. The Co K-edge EXAFS fitting results for Co-N SAC_{Mm} with different models.

Samples	S_0^2	CN	σ^2 (Å^2)	ΔE_0 (eV)	R (Å)	R-factor
pyridine-type CoN_4	0.71	3.88	0.00386	-5.90	1.90	0.0194
pyridine-type CoN_3O_1	0.71	3.88	0.00304	-1.48	1.94	0.0524
pyridine-type CoN_2O_2	0.71	3.87	0.00710	1.54	1.95	0.0394
pyridine-type CoN_4-O_A	0.71	3.88	0.00568	-3.43	1.93	0.0346
pyridine-type CoN_4-O_B	0.71	3.89	0.00226	-4.87	1.94	0.0308
pyridine-type CoN_4-O_C	0.71	3.91	0.00514	-4.95	1.90	0.0712
pyridine-type CoN_4-DF_A	0.71	3.90	0.00558	-5.52	1.91	0.0431
pyridine-type CoN_4-DF_B	0.71	3.87	0.00316	-4.81	1.92	0.0730

Screened from different theoretical models (Table S5), considering the small R-factor the pristine pyridine-type CoN_4 model shows the best fitting goodness for the Co-N SAC_{Mm} sample as compared to the CoN_4 models modified with C-O-C groups or defects.

Table S6. The Co K-edge EXAFS fitting results for Co-N SAC_{Dp}, Co-N SAC_{Pc} and Co-N SAC_{Mm}.

Samples	Path	S_0^2	CN	σ^2 (Å^2)	ΔE_0 (eV)	ΔR (Å)	R (Å)
Co foil	Co-Co	0.71	12	0.00521	6.30	-0.018	2.48
Co-N SAC_{Dp}	Co-N	0.71	3.86	0.00923	-1.55	0.045	2.02
Co-N SAC_{Pc}	Co-N	0.71	3.90	0.00611	-5.65	0.017	1.93
Co-N SAC_{Mm}	Co-N	0.71	3.88	0.00386	-5.90	0.055	1.90

S_0^2: the amplitude reduction factor (S_0^2=0.71 is determined by fitting EXAFS spectrum of Co foil).

CN: the coordination number.

σ^2: Debye-Waller factor to evaluate thermal and static disorder.

ΔE_0: inner potential correction.

ΔR: the change of the interatomic distance relative to the initial length.

R: the interatomic distance (bond length from center atom to coordination atom).

Table S7. BET surface area of the three different samples.

Samples	BET surface area (m^2/g)
Co-N SAC_{Dp}	1130
Co-N SAC_{Pc}	1016
Co-N SAC_{Mm}	1001

Table S8. The content of different elements for the three Co-N SAC samples.

Samples	N[a] (wt.%)	O[a] (wt.%)	C[a] (wt.%)
Co-N SAC_{Dp}	1.89	2.40	95.2
Co-N SAC_{Pc}	4.23	3.51	91.6
Co-N SAC_{Mm}	3.10	3.04	93.2

a: determined by elemental analyzer.

Table S9. The $E_{-0.2}$ for the different samples.

Samples	$E_{-0.2}$ (vs. RHE)
Co-N SAC_{Dp}	0.632
Co-N SAC_{Pc}	0.691
Co-N SAC_{Mm}	0.767

Table S10. The ECSA of the three different samples.

Samples	ECSA (mF cm^{-2})
Co-N SAC_{Dp}	5.0
Co-N SAC_{Pc}	5.5
Co-N SAC_{Mm}	7.2

Table S11. Comparison of the $2e^-$ ORR performance and H_2O_2 production ability with the recently reported catalysts in acid electrolyte.

Catalyst	Electrolyte	Mass Activity at 0.5 V ($A\ g^{-1}_{cat.}$)	H_2O_2 Selectivity @I_{H2O2} at 0.3 V (%@mA)	H_2O_2 Production rate ($mg\ cm^{-2}\ h^{-1}$)	Stability (h)	H_2O_2 Yield	Reference
Co-N SAC_{Dp}	**0.1 M $HClO_4$**	**14.4**	**94@0.61**	**26.7**	**90**	**2032 mg@90 h**	***This work***
Co−N−C	0.5 M H_2SO_4	8.3	76@0.41	N/A	N/A	N/A	*J. Am. Chem. Soc. 2019, 141, 12372−12381*
Co_1-NG(O)	0.1 M $HClO_4$	46	~48@0.39	N/A	10	N/A	*Nat. Mater., 2020, 19, 436-442*
CoNOC	0.1 M $HClO_4$	2.8	>95@0.48	4.02	11	3800 mg/L @11 h	*J. Am. Chem. Soc. 2021, 143, 20, 7819–7827*
EA-CoN@CNTs	0.1 M $HClO_4$	10.6	~90@0.7	N/A	12	414 mg@12 h	*Nat. Commun. (2020) 11, 4181*
$CoSe_2$	0.5 M H_2SO_4	2.77	98@0.24	30.6	100	N/A	*Angew. Chem. Int. Ed. DOI: 10.1002/anie.202111075*
o-$CoSe_2$	0.05 M H_2SO_4	10.5	~89@0.68	0.19	6	1.145 mg@6 h	*Energy Environ. Sci., 2020, 13, 4189*
{001}-Fe_2O_{3-x}	5 mM H_2SO_4	<0.31	88@0.1	N/A	27.7	N/A	*Adv. Funct. Mater. 2020, 30, 1910539*
NiS_2	0.05 M H_2SO_4	1.5	92@0.36	N/A	6	243 mg/L@ 6.67h	*J. Mater. Chem. A, 2021, 9, 6117*
$Pd^{\delta+}$-OCNT	0.1 M $HClO_4$	~11	95@0.32	-	8.33	-	*Nat. Commun. (2020) 11, 2178*
Pd/GNR	0.1 M $HClO_4$	14.6	90@0.53	N/A	N/A	N/A	*J. Phys. Chem. C 2018, 122, 15878−15885*
h-Pt_1-CuS_x	0.1 M $HClO_4$	6.5	~93@0.52	6.2	1	4.66 mg@1 h	*Chem 5, 1–12, 2019*
Au/C	0.1 M $HClO_4$	1.45	80@0.25	N/A	N/A	N/A	*Phys. Chem. Chem. Phys., 2010, 12, 8042–8052*
Pt/HSC	0.1 M $HClO_4$	2.69	~94@0.1	3.3	6	27.2 mg@ 6h	*Nat. Commun. (2016) 7, 10922*
Pt–Hg	0.1 M $HClO_4$	11.2	91@0.5	-	8,000 cycles	N/A	*Nat. Mater. 2013, 12, 1137–1143.*

Reference

1. Newville, M., IFEFFIT : interactive XAFS analysis and FEFF fitting. *J. Synchrotron Radiat.* **2001,** *8* (2), 322-324.

2. Gao, J.; Yang, H. b.; Huang, X.; Hung, S.-F.; Cai, W.; Jia, C.; Miao, S.; Chen, H. M.; Yang, X.; Huang, Y.; Zhang, T.; Liu, B., Enabling Direct H_2O_2 Production in Acidic Media through Rational Design of Transition Metal Single Atom Catalyst. *Chem* **2020,** *6* (3), 658-674.

3. Kresse, G.; Hafner, J., Ab initio molecular dynamics for liquid metals. *Phys. Rev. B* **1993,** *47* (1), 558-561.

4. Kresse, G.; Furthmüller, J., Efficient iterative schemes for ab initio total-energy calculations using a plane-wave basis set. *Phys. Rev. B* **1996,** *54* (16), 11169-11186.

5. Perdew, J. P.; Burke, K.; Ernzerhof, M., Generalized Gradient Approximation Made Simple. *Phys. Rev. Lett.* **1996,** *77* (18), 3865-3868.

6. Henkelman, G.; Jónsson, H., Improved tangent estimate in the nudged elastic band method for finding minimum energy paths and saddle points. *J. Chem. Phys.* **2000,** *113* (22), 9978-9985.

7. Tang, C.; Chen, L.; Li, H.; Li, L.; Jiao, Y.; Zheng, Y.; Xu, H.; Davey, K.; Qiao, S.-Z., Tailoring Acidic Oxygen Reduction Selectivity on Single-Atom Catalysts via Modification of First and Second Coordination Spheres. *J. Am. Chem. Soc.* **2021,** *143* (20), 7819-7827.

8. He, Y.; Shi, Q.; Shan, W.; Li, X.; Kropf, A. J.; Wegener, E. C.; Wright, J.; Karakalos, S.; Su, D.; Cullen, D. A.; Wang, G.; Myers, D. J.; Wu, G., Dynamically Unveiling Metal–Nitrogen Coordination during Thermal Activation to Design High-Efficient Atomically Dispersed CoN_4 Active Sites. *Angew. Chem. Int. Ed.* **2021,** *60* (17), 9516-9526.

9. He, Y.; Hwang, S.; Cullen, D. A.; Uddin, M. A.; Langhorst, L.; Li, B.; Karakalos, S.; Kropf, A. J.; Wegener, E. C.; Sokolowski, J.; Chen, M.; Myers, D.; Su, D.; More, K. L.; Wang, G.; Litster, S.; Wu, G., Highly active atomically dispersed CoN_4 fuel cell cathode catalysts derived from surfactant-assisted MOFs: carbon-shell confinement strategy. *Energy Environ. Sci.* **2019,** *12* (1), 250-260.

10. Wang, T.; Sun, Y.; Zhang, L.; Li, K.; Yi, Y.; Song, S.; Li, M.; Qiao, Z.-A.; Dai, S., Space-Confined Polymerization: Controlled Fabrication of Nitrogen-Doped Polymer and Carbon Microspheres with Refined Hierarchical Architectures. *Adv. Mater.* **2019,** *31* (16), 1807876.

11. Zhang, H.; Gu, W.; Ran, Q.; Gu, Y., Synthesis and Characterization of Pyridine-Based Benzoxazines and Their Carbons. *J. Macromol. Sci., A* **2014,** *51* (10), 783-787.

12. Pels, J. R.; Kapteijn, F.; Moulijn, J. A.; Zhu, Q.; Thomas, K. M., Evolution of nitrogen functionalities in carbonaceous materials during pyrolysis. *Carbon* **1995,** *33* (11), 1641-1653.

13. Zhang, S.; Tsuzuki, S.; Ueno, K.; Dokko, K.; Watanabe, M., Upper Limit of Nitrogen Content in Carbon Materials. *Angew. Chem. Int. Ed.* **2015,** *54* (4), 1302-1306.

14. Sharifi, T.; Hu, G.; Jia, X.; Wågberg, T., Formation of Active Sites for Oxygen Reduction Reactions by Transformation of Nitrogen Functionalities in Nitrogen-Doped Carbon Nanotubes. *ACS Nano* **2012,** *6* (10), 8904-8912.

15. Menga, D.; Low, J. L.; Li, Y.-S.; Arčon, I.; Koyutürk, B.; Wagner, F.; Ruiz-Zepeda, F.; Gaberšček, M.; Paulus, B.; Fellinger, T.-P., Resolving the Dilemma of Fe–N–C Catalysts by the Selective Synthesis of Tetrapyrrolic Active Sites via an Imprinting Strategy. *J. Am. Chem. Soc.* **2021,** *143* (43), 18010-18019.

16. Liu, C.; Wu, Y.; Sun, K.; Fang, J.; Huang, A.; Pan, Y.; Cheong, W.-C.; Zhuang, Z.;

Zhuang, Z.; Yuan, Q.; Xin, H. L.; Zhang, C.; Zhang, J.; Xiao, H.; Chen, C.; Li, Y., Constructing FeN_4/graphitic nitrogen atomic interface for high-efficiency electrochemical CO_2 reduction over a broad potential window. *Chem* **2021,** *7* (5), 1297-1307.
17. Li, L.; Tang, C.; Zheng, Y.; Xia, B.; Zhou, X.; Xu, H.; Qiao, S.-Z., Tailoring Selectivity of Electrochemical Hydrogen Peroxide Generation by Tunable Pyrrolic-Nitrogen-Carbon. *Adv. Energy Mater.* **2020,** *10* (21), 2000789.
18. Zhang, N.; Zhou, T.; Chen, M.; Feng, H.; Yuan, R.; Zhong, C. a.; Yan, W.; Tian, Y.; Wu, X.; Chu, W.; Wu, C.; Xie, Y., High-purity pyrrole-type FeN_4 sites as a superior oxygen reduction electrocatalyst. *Energy Environ. Sci.* **2020,** *13* (1), 111-118.
19. Jung, E.; Shin, H.; Lee, B.-H.; Efremov, V.; Lee, S.; Lee, H. S.; Kim, J.; Hooch Antink, W.; Park, S.; Lee, K.-S.; Cho, S.-P.; Yoo, J. S.; Sung, Y.-E.; Hyeon, T., Atomic-level tuning of Co–N–C catalyst for high-performance electrochemical H_2O_2 production. *Nat. Mater.* **2020,** *19* (4), 436-442.
20. Zhang, Q.; Tan, X.; Bedford, N. M.; Han, Z.; Thomsen, L.; Smith, S.; Amal, R.; Lu, X., Direct insights into the role of epoxy groups on cobalt sites for acidic H_2O_2 production. *Nat. Commun.* **2020,** *11* (1), 4181.